COLLAPSE OF SEAFLOOR VOLCANIC TERRAIN: A KEY PROCESS IN THE FORMATION OF THE UPPER OCEANIC CRUST

A THESIS SUBMITTED TO THE GRADUATE DIVISION OF THE
UNIVERSITY OF HAWAI'I IN PARTIAL FULFILLMENT
OF THE REQUIREMENTS FOR THE DEGREE OF

MASTER OF SCIENCE

IN

GEOLOGY AND GEOPHYSICS

AUGUST 2001

By
Jennifer L. Engels

Thesis Committee:

Margo Edwards, Chairperson
Frederick Duennebier
John Sinton
Daniel Fornari

We certify that we have read this dissertation and that, in our opinion, it is satisfactory in scope and quality as a dissertation for the degree of Doctor of Philosophy in Geology and Geophysics.

DISSERTATION COMMITTEE

Paul Lucey
Chairperson

B Ray Hawke

Victoria J. Hamilton

We certify that we have read this thesis and that, in our opinion, it is satisfactory in scope and quality as a thesis for the degree of Master of Science in Geology and Geophysics.

THESIS COMMITTEE

_____

Chairperson

_____

_____

_____

ACKNOWLEDGEMENTS

First and most importantly I would like to thank my parents for providing me with thought-provoking learning opportunities that ensured my continued interest in research. They consistently put creativity and open-mindedness before scholastic results, for which I am truly grateful. I would like to thank Doug Holdt for coming to Hawaii with me, and thanks to both Doug Holdt and Mary Engels for reminding me what my real priorities are.

The faculty, staff, and students of the Geology and Geophysics Department at the University of Hawaii are a vast and user-friendly repository of geologic knowledge. I am constantly re-inspired by the excitement of my peers in the department about their research projects. Thanks.

I am grateful to the crews of the R/V *Atlantis*, the DSV *Alvin*, and the R/V *Melville* for their assistance in collecting these data. Chapters 1 and 2 were a collaborative effort, and would not have been possible without the input of co-authors Margo Edwards, Dan Fornari, Mike Perfit, Greg Kurras, and Del Bohnensteil. Special thanks to Dan Scheirer and Paul Johnson for help with sonar data acquisition and processing. Dana Yoerger, Hans Schouten, and Matthew Smith provided stimulating discussions from which this research greatly benefited. This research was supported by a grant from the National Science Foundation, grants OCE-9986874. Additional support was provided by the WHOI Deep Submergence group.

ABSTRACT

Seafloor lava flows often display a wide dimensional range of void spaces within the flow that can be exposed through collapse of the surface crust. Collapse features in submarine lava flows have been observed at mid-ocean ridges throughout the world's oceans, but they have never been systematically mapped or studied. As such, no consensus exists regarding the processes responsible for the initiation, formation and geometry of volcanic collapse in the deep ocean. Despite this lack of knowledge, basic principles and our conceptual understanding of ocean crustal processes suggest that volcanic collapse provides a fundamental control on shallow hydrothermal circulation, the porosity of the upper ocean crust, extent of subsurface habitats, and lava distribution and channelization.

Visual and photographic observations using the submersible *Alvin* and a towed camera system on the East Pacific Rise at 9°37' N and 9°50'N were analyzed to describe variations in volcanic morphology and collapse as a function of spatial location along the ridge axis. Analysis of the photographic data collected from a ridge offset at 9°37'N, a segment end, and a recently active segment center at 9°50' N reveals that at both locations ~13% of the surface area of lava flows is collapsed. Collapse features and lobate lava morphologies exhibit a strong positive correlation, with 89% of all collapse occurring in lobate flows. Volcanic collapse features in my study area represent a spectrum with endmember size categories that are inferred to have genetic implications for the processes that

initiated the collapse. Small endmember collapse features expose void spaces that are typically <0.50 m deep and have diameters <2 m. Large endmember collapse features can cover 10's to 1000's of square meters, and are associated with voids in the flows that range in depth from 1-20 m. Although the amount of collapsed area at these two sites is statistically identical, the style and distribution of collapse differs markedly between the two locations. At the 9°37'N site that marks the end of a morphotectonic segment, and where magmatism is inferred to be less robust, collapse is dominated by features at the large end of the collapse spectrum. At the 9°50'N site in the center of a morphotectonic segment, where active volcanism took place in 1991, collapse is dominated by features at the small end of the collapse spectrum.

The mechanisms responsible for the initiation of small and large collapse can be inferred from the presence of delicate drip structures and patinas on the interior of lava crusts sampled from collapsed flows. This thesis presents a model that describes collapse formation.

- An envelope of water is trapped either at the flow front or beneath it and is channeled to the upper portion of the flow.
- Patinas and drip structures found on the underside of collapse roofs are formed when trapped water or magmatic volatiles flash to vapor beneath new submarine lava crusts, separating the crust from the molten interior of the lava.

- Pressure gradients across the crust caused by variations in magmatic driving pressure or local perturbations cause cracks or small collapse in the crust which allow seawater to enter beneath the now cooled crust.
- Ambient temperature bottom water on either side of a cooling lava crust prevents the still molten interior of the flow from imparting thermal stresses on the cooling crust, which would create large cooling cracks on the lobate surfaces, such as those seen in pillow lava.
- The formation of large collapse features is associated with large volume withdrawal of magma beneath an inflating lava flow either into the down-slope terminus of a lava tongue, local fissures, or the primary eruptive vent fissures.

TABLE OF CONTENTS

Acknowledgements iii

Abstract iv

List of Tables ix

List of Figures x

List of Abbreviations xi

Chapter 1: Introduction to submarine volcanic collapse 1

1.1 Prior modeling of submarine volcanic processes 3

1.2 Implications for crustal porosity 5

1.3 Hydrothermal and biological processes 6

1.4 Background to the study areas 7

1.5 Data acquisition and processing methods 10

Chapter 2: Conceptual models for collapse formation based on data from a ridge offset at 9°37'N on the East Pacific Rise 13

2.1 Observations and analyses of flow morphologies and collapse features ... 13

2.1.1 Flow morphologies 13

2.1.2 Collapse features 16

2.1.2.1 Hand samples 16

2.1.2.2 Small collapse 17

2.1.2.3 Large collapse 18

2.2 Discussion 21

2.2.1 The role of vapor in collapse initiation 21

2.2.2 The role of pre-existing topography in the formation of large collapse 28
2.3 Conclusions 31
Chapter 3: Comparison of collapse distribution and abundance at a segment center and a segment end, 9°37'N EPR and 9°50'N EPR 34
3.1 Comparative statistical analyses of flow morphologies and collapse features 34
3.1.1 Morphology types 35
3.1.2 Collapse features 36
3.2 Conclusions 41
Appendix A: Table 44
Appendix B: Figures 45
References 66

LIST OF TABLES

Table Page

1. Collapse Characteristics..... 44

LIST OF FIGURES

Figure Page

1. Location map 52
2. Sidescan and morphology of 9°37'N ridge offset 53
3. Sidescan and morphology of the 9°50'N segment center 54
4. Collapse map for 9°37'N ridge offset 55
5. Photographs of collapse 56
6. Photographs of drip structures and reaction patinas 57
7. Vapor-initiated collapse model 58
8. Model showing influence of antecedent topography on collapse .. 59
9. Morphology data histogram 60
10. Collapse type histogram 61
11. Collapse map for 9°50'N segment center 62
12. Collapse distribution comparison histograms, all collapse 63
13. Collapse distribution comparison histograms, east and west limb of 9°37'N ridge offset shown individually 64
14. Collapse distribution comparison histograms, survey box areas ... 65

LIST OF ABBREVIATIONS

1. AHA-Nemo2 – R/V Melville Nemo Expedition, Leg 2, cruise to East Pacific Rise to collect DSL-120 sidescan data, 2000
2. ALGRAV2000 – R/V Atlantis Expedition 3, Leg 47, *Alvin* cruise to collect gravity data on the East Pacific Rise, 2000
3. AML – axial magma lens
4. ARGO – visual and acoustic dataset of the East Pacific Rise collected in 1989
5. ASCT – axial summit collapse trough
6. DSL-120 – sidescan dataset with 1-2m resolution
7. Deval – deviation from axial linearity as defined by Langmuir et al. [1986]
8. EPR – East Pacific Rise
9. LBL – long-baseline transponder
10. LVZ – seismic low-velocity zone
11. Lobates – lobate lavas
12. MOR – mid-ocean ridge
13. R/V – research vessel
14. (S)OSC – (small) overlapping spreading center

WHOI-TCS – Woods Hole Oceanographic Institution towed camera system

CHAPTER 1: INTRODUCTION TO SUBMARINE VOLCANIC COLLAPSE

Seafloor lava flows, especially those erupted at intermediate to super-fast spreading mid-ocean ridges, often display a wide volumetric range of void spaces within the flow exposed through collapse of the surface crust. The smooth surfaces of lobate and sheet submarine lavas are commonly disrupted by collapse of the flow surface, but there are also wide expanses of pristine smooth lava crust that extend for tens of meters or more. These irregularly shaped "holes" in the lava crust are termed "collapse features", and the original crust of the flow is often observed as tabular, curvilinear pieces of lava crust on the floor of the collapse. Since collapse is an important component of mid-ocean ridge volcanic terrains, studying the formation of collapse features will help scientists to understand fundamental physical properties of the uppermost ocean crust such as its porosity, pathways for hydrothermal fluid flux, and the extent of subsurface habitats. Additionally, from the character and distribution of collapse features we can deduce information about seafloor eruption processes.

The global mid-ocean ridge (MOR) is the largest volcanic system on Earth, producing oceanic crust that covers ~70% of the Earth's surface. However, due to the depth (~2500-3500m) of the MOR axis and the limited areas where detecting MOR eruptions in real time is possible [Fox et al., 1999], a seafloor eruption has yet to be detected in progress. At shallow depths, the formation and down-slope flow of submarine pillows have been observed during the ocean entry of Kilauean lavas [Moore et al., 1973; Tribble, 1991]. Since nearly identical

pillow morphologies are present at both shallow oceanic island flanks and MOR environments, these observations provide useful analogs to ridge crest pillow formation. Hon et al. [1994] and Fornari [1986] compared the distribution of subaerial compound pahoehoe lavas and simple sheet flows to analogous terrains on the ocean floor and documented similar morphologies. Recent studies conducted by Gregg et al. [2000, 1995], Klingelhofer et al. [1999], Chadwick et al. [1999] and Griffiths et al. [1992] modeled the formation of different lava morphologies observed on the seafloor by varying temperature, slope and extrusion rate. However, none of these models specifically addressed the creation and maintenance of void space within the upper few meters of oceanic crust. Wax analogs of seafloor extrusion processes are unable to recreate the brittle carapaces needed to simulate collapse, and Klingelhofer et al.'s [1999] numerical modeling did not address the formation of collapse features.

Despite their ubiquitous presence along the global mid-ocean ridge (MOR), collapse features have never been systematically mapped or studied. As such, no consensus exists regarding the processes responsible for the initiation, formation and modification of volcanic collapse in the deep ocean. This thesis presents results of the first program specifically designed to characterize collapse on a fast-spreading mid-ocean ridge. The goal of my study is to document the occurrence and distribution of collapse features in the field using photographs of lava flows on the crest of the fast-spreading EPR. The investigation focuses on an ~6 km-long region around a small ridge offset at 9°37'N within a zone extending ~250 m from the ASCT (Figure 1). In describing the dimensions of collapse

features, the associated void spaces, and the physical setting in which collapse occurs, and examining in close detail some of the remnants associated with collapse, I create the first comprehensive database of collapse styles at a fast-spreading mid-ocean ridge. I then statistically characterize the distribution of collapse features relative to each other, lava morphology and geologic setting. The results are used to provide first-order models for the processes that control collapse initiation, formation and modification and to discuss the implications that collapse features have for shallow hydrothermal circulation, the porosity of the uppermost ocean crust, the extent of subsurface habitats, and lava distribution and channelization.

1.1 Prior Modeling of Submarine Volcanic Processes

Wax modeling experiments that simulate the extrusion and cooling of basaltic magmas allowed Gregg et al. [2000, 1995], Chadwick et al. [1999] and Griffiths and Fink [1992] to develop useful models of submarine eruptions. These studies investigated the influence of lava effusion, cooling and solidification rates, as well as antecedent slope, on the dynamics and morphology of submarine flows. Although it is difficult to scale the results of these experiments to the dimensions, material properties and complex emplacement histories of lava observed on the ocean floor, they provide a first-order quantification and conceptual understanding of the processes involved, and some indication as to which parameters may be most influential. Klingelhofer et al. [1999] demonstrated that a multi-parametric numerical model can describe pillow

and sheet flow lavas while taking into account common variations in basaltic rheology based on composition. Their results indicate that lava viscosity and the driving pressure gradient are the most important factors influencing the flow rate, geometry and morphology of submarine lava flows. Chadwick et al. [1999] created a detailed conceptual model for the subsidence of lava ponds, and Gregg et al. [2000] described the formation of lava pillars. Neither study, however, discusses the implications of volcanic collapse for creating a wide volumetric range of porosity in lava flows that form the upper ocean crust.

Collapse of volcanic terrain has been observed to various extents at all MOR sites studied using submersibles or deep sea cameras although it appears to be most prevalent at fast-spreading ridges where lobate and sheet lava predominate and effusion rates are high. In the first detailed report of submarine collapse, Ballard et al. [1979] describe collapse pits on the intermediate-spreading rate Galapagos Rift. They noted the similarity between caverns, roof overhangs and ribbed terraces found in the bounding walls of large submarine collapse pits and features formed as a result of subaerial eruptions. Based on the similarities in morphology, Ballard et al. [1979] suggested that submarine collapse, like its subaerial counterpart, results from drain-away of still-molten lava within large lava ponds below a cooled surface crust. In Hawaii and Iceland withdrawal of magma back into the eruptive fissure is commonly observed at the ends of eruptions [*Wolfe et al.*, 1988, *Wadge et al.*, 1981]. Magmatic withdrawal or "drain-away" is a viable mechanism for creating many large submarine collapse features characterized by void spaces that are meters in depth including those

observed at the 9°37'N ridge offset and 9°50'N segment center; however, a significant percentage of collapse features found along the global MOR are quite small, affecting sub-meter areas within individual flow lobes, sheets or pillows [*Lonsdale*, 1977], and exhibiting void spaces only a few centimeters deep. These small collapse features show no direct association with eruptive fissures and often are observed to occur at the distal ends of lava flows where drain-away is unlikely to occur. The apparent inability of the lava inflation and subsequent drain-away model to explain the existence of small-scale collapse underscores the fact that the full spectrum of collapse features observed on MORs has not been systematically described. Until the style and occurrence of collapse are documented and studied, models describing the collapse in seafloor lava flows will be incomplete.

1.2 Implications for Crustal Porosity

Water-filled void space in the upper part of the oceanic crust is hypothesized to exist based on the results of seismic reflection profiles and near-bottom gravity anomalies [*Christenson et al.*, 1992; Vera et al., 1994; Cochran et al., 1999; Yoerger et al., 2000]. Christenson et al. [1992] show that the uppermost section of young oceanic crust found at MORs consists of a series of seismically distinct layers. At the EPR near 9°30'N Christenson et al. [1992] determined that the uppermost 60 m of the crust associated with the ASCT and extending 1 km to either side of the trough has very low seismic velocities (~1.95 km/s). From 60-160 m depth the seismic velocities are ~4.2 km/s; velocities increase to 5.0 km/s below 160 m. The geometry of these low velocity layers suggests they extend

uniformly along axis, are coincident with the location of the ASCT, and are present out to ~2-4 km to either side of the axis, where Layer 2A more than doubles in thickness. Vera et al. [1994] hypothesized that the seismic low-velocity zone (LVZ) can be explained by ~20% large-scale porosity in the upper crustal layer caused by low aspect ratio fractures within the extrusive volcanics. However, studies by Shah et al. [1999] and Schouten et al. [1999] indicate zones of low magnetization at the crest of fast-spreading ridges are strongly correlated with lava conduits and tubes whose locations are known from observations of surficial submarine collapse features and detailed near-bottom sonar images. Shah et al. [1999] infer that magnetization lows throughout the ridge crest can be attributed to large void spaces in the shallow crustal extrusive layer, created by subsurface conduits through which lava is transported away from axis.

1.3 Hydrothermal and Biological Processes

Hydrothermal circulation in the ocean crust requires effective permeability throughout the crustal section. Ridge parallel fractures associated with normal faults are often called upon to provide the deep fracture system that permits inflow of seawater to the reaction zone as well as pathways for upwelling limbs of the circulation cells [e.g. Humphris, 1995; Fornari and Embley, 1995; Kleinrock and Humphris, 1997]. Along-axis distribution of hydrothermal vent fields has been attributed to both segmentation of the MOR crest at 3rd and 4th order discontinuities [*Macdonald et al.*, 1992] as well as to variations in shallow crustal permeability structure developed as a result of primary volcanic transport systems

distributing lava along and across the ridge crest [Haymon et al., 1991; Fornari and Embley, 1995; Haymon, 1996]. The presence of vugular porosity within the crust as a result of large and small-scale collapse within individual lava flows provides excellent potential to enhance the permeability structure of the crust. In addition, this intraflow permeability afforded by collapse features creates subsurface micro- and macrobiological habitats which may play a fundamental role in maintaining and distributing hydrothermal fauna in between and during seafloor eruptions [Delaney et al., 1998]

1.4 Background to the study areas, 9°37'N and 9°50'N EPR

This thesis characterizes collapse at a 450 m right-stepping offset in the ASCT on the fast-spreading EPR (Figures 1 and 2), at the end of a morphotectonically defined segment (11 cm/yr full rate [*Klitgord and Mammerickx,* 1982*; Carbotte and Macdonald,* 1992]). Water depth at the site, which was investigated using ArgoII in 1989, DSL-120 in 2000, and the *Alvin* submersible plus various towed camera systems in 1991, 1994 and 2000, ranges from 2550 m to 2590 m. The width of the ASCT varies from a few tens of meters at the overlapping tips to >250 m at 9°38'N. In general, the width of the eastern ASCT limb is greater and more variable in plan-view than the width of the western limb.

The influence of the ridge offset at 9°37'N relative to broad-scale EPR segmentation is presently under debate. Differences in lava age, hydrothermal vent fluids and fissure abundance have been documented to the north and south of

this offset [*Wright et al.,* 1995*; Fornari et al.,* 1998*; Von Damm,* 2000*; Smith et al.,* in press]. Due to the lack of active vents or associated biota seen during the 1989 ArgoII survey, Haymon et al. [1991] described the 9°37'N offset as a 4th order ridge discontinuity and hydrothermal gap. A local minimum in cumulate fissure width led Wright et al. [1995] to suggest the area may recently have been volcanically active. Smith et al. [in press] differentiate inferred lava age, fissure density, fissure width, morphology and magmatic signature to the north and south of the ridge offset, while comparing the activity and temperature of sulfide vent edifices in the dying (western) and propagating (eastern) limb. They conclude that this small ridge offset is a 3rd order discontinuity as well as a magmatic and hydrothermal boundary. The combined data from Haymon et al. [1991,1993], Wright et al. [1995] and Smith et al. [in press] suggest that the eastern limb of the ridge offset is extending south and that the center of eruptive activity may have propagated up to 500 m south since the first high-resolution ArgoII survey conducted over 10 years ago.

The second study area is centered on a recently volcanically active site on the EPR at 9°50'N [*Haymon et al.*, 1993, *Rubin et al.*, 1994](Figure 3). The tectonic regime has been defined as a 4th order morphotectonic segment by Haymon et al. [1991], and categorized as one of the youngest segments between 9°09'N-9°54'N based on an abundance of glassy, unsedimented lavas and a narrow, shallow ASCT (40-70 m wide). Additionally, it is the site of the largest number of high temperature hydrothermal vents documented in the 1989 ArgoII survey [*Haymon et al.,* 1991]. Vera and Diebold's [1994] study of seismic layer

2A and depth to the axial melt lens (AML) shows that the AML at this location reaches its shallowest depths between 9°-10° N at ~1400 m below the seafloor, as opposed to ~1550 m deep below the 9°37'N ridge offset.

The 9°50'N EPR site was the subject of an intensive and well-organized series of studies following detection of an in-progress eruption at the ridge crest in 1991 [*Haymon et al.,* 1993]. The ridge crest at this location had previously been surveyed by ArgoII in 1989, which provided a baseline dataset for detecting short-term changes in the appearance and behavior of the axis post-eruption. The site has since been the subject of several comprehensive sidescan, bathymetric, magnetic, hydrothermal, and petrologic mapping studies, including those by Haymon et al. [1991, 1993], Wright et al. [1995], Fornari et al. [1998], Schouten et al. [1999], Sohn et al. [1999], Kurras et al. [2000], Von Damm [2000], and the AHA-Nemo2 cruise [D. Fornari, pers. commun., 2001]. Kurras et al. [2000] described the morphologic character of lavas extending off axis across the zone where layer 2A more than doubles in thickness, and concluded that pillow lavas increase with distance from the ASCT. They additionally note three dominant morphologic types along the ridge crest, including lobate, sheet, and pillow lavas in order of decreasing abundance, and conclude that the dominance of pillow lavas off axis results from geologic factors other than lava chemistry or temperature. Off axis volcanism at this site is interpreted to result from events that are not coincident with eruptions in the ASCT [*Kurras et al.*, 2000].

The 9°50'N EPR 4th order segment center site, and the 9°37' N ridge offset are well-suited to a systematic comparison of morphologic and collapse

features due to their location at the center and end of morphotectonic segments of the same spreading rate, within the same 2nd order segment [*Haymon et al.*, 1991]. Differences in recent eruptive activity, depth, geometry and dimensions of the ASCT, and depth to the top of the AML (~1400m at 9°50'N vs. ~1550m at 9°37'N) may account for differences in volcanic morphology and collapse features between the two sites. Additionally, observed differences in the topography of the ASCT at 9°50'N and 9°37'N may provide the basis for developing a conceptual model for the relationship between ridge crest eruptive products and collapse features.

1.5 Data Acquisition and Processing Methods

Seafloor photographic data were acquired from the 9°37'N and 9°50'N EPR areas using DSV *Alvin* video cameras and the Woods Hole Oceanographic Institution's (WHOI) towed camera sled (TCS) [*Fornari and Spencer*, 1997; *Fornari et al.*, 1998]. *Alvin* dives were designed to collect near-bottom gravity and magnetic data along E-W transects across the EPR summit at 9°37'N. The survey covered over ~6 km of along-axis terrain where the axial troughs overlap and change character from a narrow ~100-150 m-wide trough north of the ridge offset to a ~300 m-wide trough south of the overlap zone [*Yoerger et al.*, 2000]. The WHOI-TCS took digital photographs every 15 seconds at altitudes of 5-7 m above the seafloor (as determined by a 12 kHz pinger trace) along generally N-S survey lines (Figure 2). The sled was towed at ~0.25 knot, which, when combined with the 4-6 m footprint of each of the sled's photographs, yields 80-

90% coverage of the ocean floor in the along-track direction. At 9°37'N, the sled was navigated using a long-baseline (LBL) transponder network that accurately located the photographic images to within 4-5 m. Survey lines were run parallel to the ASCT every 25 m on the eastern and western ridge flanks. At 9°50'N, the sled was navigated using a layback calculation and P-Code GPS positions of the surface ship every 15 seconds. Typical camera layback during the surveys was found to be 100-200 m behind the ship. Survey lines were run parallel to the ASCT on the eastern and western ridge flanks.

Alvin video footage was collected during a series of six dives which traversed the seafloor continuously at the 9°37'N site, at a speed of ~0.5 kt and an altitude of ~5-8 m. Survey lines were separated by ~150 m and navigated using the same long-baseline transponder network as the TCS (Figure 2). However, *Alvin* navigation was enhanced by using an RDI bottom-lock Doppler [*Whitcomb et al.*, 1999]. The LBL and bottom-lock Doppler were combined to produce navigation for *Alvin* with relative positional accuracy of 1-2 m.

Alvin video data also were sampled every 15 s and together with the WHOI-TCS data analyzed using the same methods to produce information on lava flow morphologies and collapse characteristics. Each photograph or freeze-frame image was catalogued according to lava type, glassiness (a proxy for relative age), the style and extent of collapse, amount of sediment covering the surfaces of the flow, presence of biota, location relative to the ASCT, and width and distribution of fissures. Each frame was geographically referenced to study the distribution of morphologies and collapse features relative to each other and to

endemic features on the EPR crest. This technique is similar to that used by Kurras et al. [2000] and other detailed studies of seafloor volcanic geology [e.g., *Ballard et al.*, 1979; *Lonsdale et al.*, 1980; *Chadwick et al.*, 1999].

Three swaths of DSL-120 sidescan data were collected at the 9°37'N ridge offset, and two swaths were collected at the 9°50'N site in March 2000 on the AHA-Nemo2 cruise on board R/V Melville [*Scheirer et al.*, 2000]. Sidescan swaths are 1 km wide and have a pixel resolution of 1-2 m [*Stewart et al*, 1994; *Scheirer et al.*, 2000]. The resolution of the sonar data has been tested by correlating identifiable features from the bottom photographs with the sidescan imagery. These tests show a high level of correlation between the sonar data and photo imagery on features as small as 2 m in diameter.

CHAPTER 2: CONCEPTUAL MODELS FOR COLLAPSE INITIATION, FORMATION, AND EVOLUTION BASED ON DATA FROM A RIDGE OFFSET AT 9°37'N ON THE EPR

2.1 Observations and Analyses of Flow Morphologies and Collapse Features

Photographic and sidescan data were used to examine the distribution of flow morphologies relative to the two limbs of the 9°37'N ridge offset. The morphologic information was then used as a context for presenting the distribution of collapse features. The spatial distribution of collapse endmember sizes, and their co-occurrence with an identifiable suite of geologic flow textures allows me to characterize collapse features with respect to lava emplacement mechanisms. Examination of collapse roof hand samples collected from the Northern EPR gave me insight into eruption processes at the interface between molten lava flows and ambient seawater.

2.1.1 Flow Morphologies

Lobate flows (hereinafter termed "lobates") dominate the terrain around the 9°37'N ridge offset and comprise 70% of the morphologies observed (Figure 2). Lobates form oblate lobes with smooth surfaces ranging in size from a few centimeters to ~4 m across. Individual lobes have low relief (usually less than 1 m). Lobates are commonly associated with "inflation" features such as submarine tumuli, lava domes and collapse features [e.g., *Appelgate et al.*, 1991, *White et al.*, 2000]. In my field area, lobates are associated with both limbs of the ridge offset.

They are absent only in two regions of the ridge crest: (1) at both limbs of the ridge offset along the ASCT floor where collapse talus and hackly lava dominate, and (2) in an area measuring ~0.8 km^2 at the southern tip of the propagating (eastern) limb of the ridge offset where a hackly sheet flow, the youngest lava in the entire survey area, was observed [*Smith et al.*, in press].

Flat sheets, lineated sheets, ropy sheets and hackly sheet flows, together totaling 25% of the morphologies catalogued at my survey area, show a continuum of surface textures that include parallel lineations with convex or concave relief, gentle folds, onlapping folds, ropes, braided ropes, and auto-brecciated ropes and folds. These types of submarine volcanic surface textures and models for their genesis have been discussed by Chadwick et al. [1999]. The distribution of hackly sheet flows in the survey area is concentrated close to or in the ASCT, with other sheet flow morphologies present only in small areas outside the ASCT and on the upper flank of the ridge crest.

Pillow lava represents only 3% of the total volcanic morphologies imaged, forming near-spherical to flattened ellipsoid shapes. Most are typified by cooling fractures and "toothpaste" grooving from viscous lava squeezing past the jagged surfaces of cooled crusts. Linear pillow ridges and domes 5-10 m tall are situated along the eastern flank of the axis within 100 m of the ASCT and are similar to pillow mounds documented by White et al. [2000]. The pillow ridges extend ~1.8 km north and 0.6 km south of the ridge offset and are not matched by similar features on the western side of the ridge offset. Small areas of pillow lava were

observed during *Alvin* dives in the overlap area between the two axial troughs [M. Perfit and M. Smith, pers. commun., 2001].

Areas showing transitions from one flow type to another represent 2% of the total morphologies seen at the 9°37' N site. It is difficult to unambiguously determine whether these boundaries occur within a single flow or between two different flows. In some instances, separate flows can be identified by changes in sediment cover. However, the tendency of ponded flows to collect sediment, while lobe tops, pillows and hackly sheet flows allow sediment to slough off their surfaces, results in this being a poor single indicator of relative flow age [*Ballard et al.*, 1979].

The least abundant seafloor morphology commonly found either within the ASCT or on the flanks of the EPR summit includes active and inactive hydrothermal vent structures and related sediments. This morphology comprises <1% of the morphologies observed at the 9°37'N site and consists of sulfide chimneys that are usually associated with flocular hydrothermal sediments and cindery vent debris. Interestingly, 16 of the 19 vent constructs in the 9°37'N area are associated with the western, dying limb of the ASCT, while only three are associated with the eastern propagating limb. Diffuse hydrothermal venting has been documented at the three vents on the eastern limb [*Haymon et al.*, 1991; *Von Damm et al.*, 2000; *Smith et al.*, in press], but the vents on the western limb are currently inactive.

2.1.2 Collapse Features

The second half of this study involves examining the role of collapse in creating void space within the upper oceanic crust. To understand the processes that cause collapse, I cataloged the distribution and style of collapse around the 9°37'N ridge offset and grouped them according to size, depth and location relative to the ridge crest. Fine-scale changes in collapse style are tabulated for each geographically referenced image collected during the surveys based on the depth and areal coverage of the collapse feature present. My analysis of the photographic data indicates that 13% of the surface area of lava flows surveyed exhibits collapse. My analysis also suggests that there is a continuum of intermediate to large-size collapse features that are >~2 m to tens of meters across and >0.5 m deep for collapsed lava lakes. This large collapse contrasts with collapse features measuring <<0.5 m in depth and <2 m in diameter termed small collapse. Both large and small collapses have important implications for the porosity of the upper crust and the permeability structure of seafloor volcanic terrain.

2.1.2.1 Hand Samples

A number of physical characteristics are commonly observed on the undersides of lobate crusts and more rarely under sheet flows associated with collapse features. The following features have been observed to occur singularly or in various combinations on the undersides of lobate crusts sampled on the Northern EPR:

1.) Smooth textured, concave-up surfaces (Figure 6a,c).

2.) Surfaces that range from having a dull to waxy, oxidized patina [Perfit, Ridley, and Fornari, pers. commun., 2001] or a "frothy" appearance due to the concentration of microvesicles (Figure 6c).

3.) Typically, the undersides have only thin (< a few mm) glassy rinds and lack the thicker, vitreous appearance of the surface of the flows (Figure 6a,b,c).

4.) Drip-like protrusions (generally <2 cm long) that thin downward from the underside of the flow (Figure 6a,b). Evidence of lava having dripped onto underlying flows also has been noted.

5.) Thin, flange-like to cuspate structures that appear to be the walls of lava bubbles (Figure 6a). In at least one instance, a sample was recovered with an intact bubble approximately 3 cm in diameter that was filled with fluid.

2.1.2.2 Small Collapse

Small collapse consists of broken, thin lava crusts where the opening across the collapse is usually <2 m and only a few millimeters to <~0.5 m deep (Table 1, Figure 4). Small collapse represents 8% of the total collapsed surface area documented in my photographic data. This collapse style is observed in 95% of the data in lobate lavas and is mainly seen where an isolated inflation blister or the surface of the flow has collapsed locally (Figure 5).

The fact that lava flow surfaces, especially lobate and sheet flows, are smooth is somewhat paradoxical. If the interior of the flows is solid, then cracks should develop as a result of cooling stresses imparted on the crust (which is in contact with ambient ~2-4 °C bottom water) by the hot interior of the flow. My observational data show that in many cases flow surfaces are smooth and un-cracked for tens of meters along the flow length and that where cracks do exist they are usually in the form of small collapse. Small collapse features observed from *Alvin* consist of jagged pieces of a thin (~0.5-~2 cm thick) lava crust that are collapsed into a shallow hole beneath the flow surface. Often, one can see the solid interior of the flow on which the collapsed fragments are resting, like pieces of a puzzle. Delicate drip and flow structures (Figure 6a,b,c) are common on the underside of the lava crusts.

2.1.2.3 Large Collapse

Large collapse features on the EPR form jagged holes in the flow surface >2 m in diameter and range in size up to 10s-100s of meters in diameter. Lava lakes [e.g. Ballard et al., 1979] or the ASCT [e.g Fornari et al., 1998] are typical of large submarine volcanic collapse features, while smaller "large" collapse features are usually 2-5 m in diameter and are the unroofed portions of lava tubes or conduits. Unlike small-scale collapse features, large collapse is distinguished by depths of penetration that are usually > 0.5 m and can be as deep as ~10-20 m, especially in the ASCT and larger lava lakes. I categorized the different types of large-scale collapse morphologically as: skylight collapse, bridge collapse, roof

collapse, multi-story collapse and pervasive collapse. All large collapse styles are grouped in a single category totaling 92% of the collapsed surface area.

Skylight collapse represents 30% of the large-scale collapse seen at the 9°37' N site, and manifests as jagged windows into void spaces >0.5 m deep. It occurs in 97% of the data in lobate lavas (Table 1). In many instances, groups of small skylights (<1 m in diameter) give a Swiss-cheese texture to the upper flow surface. Skylights often have a sub-circular shape and do not conform morphologically to individual lobe outlines in the way that small collapse does. An extensive collection of samples from the northern and southern EPR yields a thickness range of ~4-10 cm for lava crusts recovered from the rims of skylights.

Bridge collapse comprises 4% of the large-scale collapse I observed. It consists of seemingly delicate spans of free-standing roof material separating large skylights and fields of pervasive collapse and occurs in 99% of the data in lobate lavas (Table 1). Bridges are supported over void spaces ranging in depth from 10s of cm to 1-2 m. Bridges represent a collapse stage intermediate between skylights and full-scale roof collapse (Figure 5) and are concentrated 100 m to either side of the ASCT.

Full-scale roof collapse represents 31% of large collapse mapped at the 9°37'N ridge offset. This type of collapse provides an unobstructed view of the underlying conduit and is commonly associated with fields of lava pillars. It is very common to see large tabular to curvilinear fragments of collapsed roof crusts scattered on the conduit floor. This collapse style occurs in 90% of the data in lobate lavas. Full-scale collapse occurs in 8% of the data in association with

hackly sheet flows that are the dominant lava type associated with the ASCT floor (Table 1). Roof collapse exposes void spaces that range in depth from 0.5 m to >5 m. Like bridge collapse, roof collapse is concentrated within 100 m to either side of the ASCT.

The most extensive collapse style documented at this site is termed pervasive collapse. It comprises 17% of the total large collapse observed and occurs almost exclusively, >99% frequency, in lobate lava (Table 1). In these areas, no remnant of the original roof morphology remains standing, but the floor of the void space is typically carpeted with tabular, jagged pieces that appear to have fallen from the collapsed roof. Many of these fragments are hexagonal in shape; some appear to have fallen in close proximity to their original roof neighbors, while others are jumbled and broken beyond recognition. The fields of collapsed crusts associated with pervasive collapse may be several meters to 100s of meters across and up to 20m deep. In some places, the floor below the collapsed roof shows flow textures, including channels and small levees suggesting that the flow beneath the roof was active for some time before collapse occurred. In these areas only minor intact remnants of the original roof structure are preserved, and these are mainly found attached as lava selvages to free-standing lava pillars along the margins of the collapse feature [*Gregg et al.*, 2000]. The occurrence of lava pillars is common in areas of pervasive collapse. The association of pervasive collapse with lineated sheet flows has also been observed in other MOR areas [e.g., *Chadwick et al.*, 1999].

Multi-story collapse is the least common and most penetrative collapse type along the ridge crest. It represents only 2% of the collapse types seen in my study area and consists of two or more instances of collapse exposed on top of each other at a single site (Table 1, Figure 5). Multi-story collapse is typically made up of nested skylights, a combined roof and skylight or, less commonly, vertically offset selvages that produce a "bathtub ring" effect. This style of collapse is closely associated with the ASCT and rarely is seen outside of it. Accordingly, it is associated with lobate lavas in 52% of the images and in 30% of the images with hackly sheet flows at the base of the ASCT. Based on *Alvin*'s altimeter and the pinger trace for the WHOI-TCS, multi-story collapse features reveal water filled spaces that have depths ranging up to 20 m.

2.2 Discussion

2.2.1 The role of vapor in collapse initiation

Lobate lava flows are distinguished by their very smooth, generally unbroken upper surfaces when compared to pillow and sheet flows. The smooth surfaces of lobate flows imply a decoupling between the cooled surface crust that is in contact with ambient bottom temperature seawater, and the molten interior of the flow, otherwise cracking of the crust would occur in response to thermal stresses. How this decoupling is accomplished remains speculative, but drip structures, surface textures such as quenched glassy rinds, and patinas preserved on the underside of lobate crusts (Figure 6a,b,c) suggest that vapor is likely to be

a critical component in the formation of some collapse features. In the model we detail below, fluids flashed to steam are the medium physically separating the molten interior of the flow from the thin, newly-formed outer crust of the lava flow (Figure 7).

The rough and porous terrain typical of the ASCT is infiltrated with seawater. Assuming the large-scale crustal porosity at 9°37' N is 20% [*Vera et al.*, 1994], an area 100 m by 100 m on the ASCT that extends 5 m into the subsurface would contain ~10,000 m^3 of seawater. This reservoir of seawater undoubtedly is perturbed during an eruption and lava flowing over the pre-existing volcanic carapace cannot avoid interacting with seawater. On land pahoehoe flow fronts have been observed to travel at speeds exceeding 25 m/hr [*Rowland et al.*, 1990]. In submarine environments enhanced cooling and crystallization of flow surfaces presumably slow the advance of lava; however flow speeds could still be fast enough to trap water in reservoirs beneath the flow. Submarine flow speeds are inferred from flow surface textures such as striated, hackly, and ropy sheet flows. Water heated by the eruption is forced upward, as evidenced by the occurrence of submarine pipe vesicles and lava pillars (Figure 6d and Figure 5h)[*Gregg et al.*, 2000]. Haymon et al. [1993] document an apparent hydromagmatic explosive event that occurred as a result of the rapid heating and expansion of seawater from a black smoker at Tubeworm BBQ over-run by lava during the 1991 eruption along this segment of the EPR.

In order for drips, bubbles and flanges to form beneath lobate flow surfaces, at least a few mm-cm of void space must have existed to allow space for

the drips to propagate, and temperatures must have been hot enough to allow the lava to continue to flow as a non-viscous fluid, rather than quench into brittle glass. Times for formation of the first solid lava in ambient bottom temperature seawater have been calculated experimentally by Griffiths and Fink [1992] and Gregg and Fink [1995]. They determine that eruption temperature and rate of heat loss from the surface of the flow are the two primary controls on lava cooling and solidification. In a series of experiments, they demonstrate that average times of cooling of normal MOR basalts heated to 1150°C range from 0.14 s-0.04 s when extruded into seawater with temperatures raised by the eruption to 7°C. It is clear from the experiments of Griffiths and Fink [1992] and Gregg and Fink [1995] that if molten lava is in contact with seawater, it cannot form drip structures due to the speeds at which lava quenches in water. In order to form drip structures, lava must be surrounded by a medium that can sustain temperatures of 1100°C and greater and pressures of ~300 bar, far exceeding the critical temperature of water at 300 bar which is only 400°C. The bubble-like walls and drip structures preserved in the lava of collapse roofs suggest that a fluid or vapor phase coexisited with and thermally insulated lava that was still hot enough to flow. The oxidized appearance of the interior surface of collapse roofs, lack of quenched glass, and concentrations of microvesicles on the undersides suggests significant interaction between the fluid/vapor and lava at near magmatic temperatures.

Even at depths of 2500 m, seawater surrounded by ~1200°C lava will transform to superheated steam (vapor) or a two-phase fluid (liquid plus vapor)

when its temperature passes the critical point (400°C at 300 bars pressure) depending on the relative masses of water and magma [*Morrissey et al.*, 2000]. Such superheating will result in significant volumetric expansion of the entrained water that could lead to swelling of the upper surface of flows or cracking of more rigid, glassy crusts to release the pressure. Whether and how much magmatic gas may be involved during the eruptive process is difficult to estimate. Recent evidence of direct mineral growth as sublimates from high temperature magmatic gases (500-1180°C) interacting with melt in cavities in basalts from the Mid-Atlantic Ridge and Juan de Fuca Ridge suggests magmatic gases could also be an important component of the vapor phase [*Sharopov et al.*, 2001]. Temperatures of this order seem reasonable because hydrothermal fluids from vents in this region are > 400°C [*Von Damm*, 2000].

Regardless of the ultimate origin of the fluid/vapor phase, I hypothesize that it is unable to escape through the intact frozen crust of the flow and consequently creates a pressurized boundary layer of vapor-filled void space between the quenched crust and the molten interior of the flow. The pressure within this superheated pocket of fluid/vapor allows the molten flow to decouple from the cooled roof without the roof collapsing, as long as the vapor pressure, combined with the roof strength, balances the overburden pressure of seawater (Figure 7). If the vapor pressure becomes too great a phreatomagmatic eruption would occur, but evidence for this style of volcanism has not been observed (or recognized) within the lobate flow fields at the 9°37' N site. The pocket of void space occupied solely by fluid/vapor remains open long enough for delicate lava

drip and flange structures a few cm in length to form (Figure 6a,b, Figure 7). Seawater heated past the critical phase and flashed to steam could remain hot enough to allow the molten lava to drip into the cavity and to cause spheroidal, bubble-like structures to form.

Further support for this type of process comes from the results of thermal explosion experiments to study the effects of water-magma interaction [*Wohletz*, 1983; *Morrissey et al.*, 2000]. These studies showed that Rayleigh-Taylor fluid instabilities can form at the vapor-melt contact in low viscosity melts resulting in fluidal surface textures that include moss-like, spheroidal, drop-shaped or ribbon-like features. These delicate features can be destroyed by fragmentation when vapor penetrates the melt or from the turbulence of superheated vapor film (including vapor collapse during cooling) along the magma surface. The similarity of the textures formed in the experiments and those observed on the undersides of many lava flows provides strong evidence that such a process is operative during submarine eruptions. The absence of these characteristic features as well as a lack of quenched glass in many of my samples may be a consequence of fragmentation of the quenched melt by stresses generated by rapid vapor expansion [*Morrissey et al.*, 2000] in the enclosed void space beneath the flow surface. Geochemical investigations are in progress to determine if seawater and/or magmatic volatiles have chemically interacted with the 9°37' N lavas [Perfit, Ridley, and Fornari, pers. commun., 2001].

I hypothesize that the small-scale collapse evident at 9°37' N (and by analogy, along much of the EPR, including the 9°50'N segment center) is almost

exclusively the result of the interplay between lava flow dynamics and cooling and vapor formation. The initial vapor pressure resulting from the interaction of seawater and molten lava is presumed to be great enough to balance hydrostatic pressure, but with cooling and waning pressure within the cavity, the roof above the void space becomes susceptible to collapse (Figure 7). If the pressure within the cavity increases, for example because of another eruptive pulse, the vapor pocket may act as the locus of a breakout, in part due to an increase in vapor pressure with increased temperature. Alternatively, if seawater infiltrates the flow system, it could lead to rapid condensation of the vapor phase resulting in local implosion and collapse of the thin upper lobate crust. If the void network is open enough, seawater entering the flow at one collapse point may migrate to fill other cavities with water before any part of the roof collapses. This is a plausible explanation for the large expanses of uncollapsed and uncracked lobate surfaces commonly observed at MOR crests. The seawater would equalize pressures above and below the uncollapsed remnants of the roof (Figure 7). The small collapse at 9°37' N occurs in 95% of the data within single lobes or fields of lobes near the ridge crest. Vapor trapped beneath a lobate crust will rise to the highest point of its enclosure, and accordingly I observe that small collapse features typically manifest at the projected apex of lobate lobes and are subcircular in form. The roof remnants exposed by small collapse voids are typically <4 cm thick. The majority of lobate roof samples recovered from small collapse settings also exhibit drip structures and patinas consistent with vapor pocket thermal regimes (Figure 6a,b,c). Though only 8% of the collapsed lobate surfaces

observed at the 9°37' N site show small collapse, the smooth, oblate surfaces that typify lobate lavas may conceal intact void spaces that have not collapsed, but which during formation of the lobe were filled with a heated vapor phase that insulated the roof and prevented the upper surface of the flow from cracking. Existence of these void spaces is inferred from the crack-free, inflated quality of the lobate skins. If uncollapsed lobes conceal water-filled void spaces, the roofs covering them must have enough structural integrity to have allowed them to remain intact as magmatic and vapor pressure waned.

The mechanical breaking of a roof over a large void space may initiate via a similar mechanism to that presented for small collapse. Trapped water vapor may form isolated bubbles between molten lava and quenched crusts within large lava-filled tubes or ponds. As the roof crust cools, it thickens inward, except where vapor pockets thermally insulate the crystallizing carapace and slow the inward propagation of the lava solidification front (Figure 8). The roof above vapor pockets could therefore be thinner than roof coupled to magma. As the molten lava below the roof starts to lower due to drain-away or contraction from cooling, the vapor pressure dissipates, leaving a weak point in the roof structure at the site of the vapor pocket. The roof breaks at this location, allowing seawater to infiltrate the tube or pond, and sometimes initiating collapse of the entire roof structure. I propose that vapor pocket collapse over large void spaces creates isolated collapse features such as the small skylights observed at 9°37' N (Figure 8). However, the distinctive morphologic differences between most small and

large collapse features suggest that additional processes contribute to the formation of large collapse.

2.2.2 The role of pre-existing topography in the formation of large collapse

Small collapse is evenly distributed over the ridge crest and flanks at 9°37' N, but large collapse increases in breadth close to the ASCT. Large collapse features within the ASCT can measure from 10-20 m deep, and are clearly linked to the formation and propagation of the ASCT itself. Very large collapse features are commonly associated with lava lakes, which most often occur in the ASCT, but can also be found off axis. Collapse features that expose lava distributary systems, such as skylight, bridge, and roof collapse, are rarely greater than 5 m deep, and are present at the axis and up to ~200 m to either side. I hypothesize that most large collapse features are formed by massive drain-away of the molten lava that supports collapse roofs, but the mechanical processes that trigger collapse also are influenced by the distribution of pillars and walls supporting the roof structure (Figure 8).

Eruptions on the EPR typically initiate through dike-related fractures at the base of the ASCT or on the ridge flanks. Commonly the first vigorous pulse of the eruption extrudes hot, low-viscosity lava in sheets or lobes along the floor of the ASCT [*Kurras et al.,* 2000; *Gregg et al.*, 1995, *Wolfe et al.*, 1988, *Wadge et al.*, 1981]. Fresh lava becomes topographically confined or stagnates in contact with seawater, either within the ASCT or within conduits on the ridge flanks [*Gregg et al.*, 1995, *Griffiths and Fink*, 1992]. Depending on the volume and

effusion rate of the flow, continued injection of magma can cause the flow to inflate *in situ*, until either the eruption volume reaches a maximum or the pressure of the underlying molten lava causes a breakout from the inflated carapace (Figure 8). When the eruption wanes or ceases, gravity causes drain-away of the pooled lava. Lava may drain back into the original eruptive fissure or into a subsurface tube system. The evacuation of lava leaves a characteristic cavern-like void space that is a necessary component for producing the large-scale collapse observed at 9°37' N.

The susceptibility of a thick roof over a large void space to collapse is dependent on two factors: 1.) the amount of structural weakening the roof has sustained due to thermal contraction or thinning resulting from the presence of vapor pockets, and 2.) the thickness of the roof relative to the expanse over which it is supported from below by pillars and the bounding walls of the void space. Roof thickness is a function of the time the molten lava has remained in contact with seawater. A thick and uncracked roof, or a roof supported at closely spaced intervals by pillars or bounding walls, may remain intact throughout the drain-away process. If the roof is thin, fractured, or unsupported over large distances, catastrophic collapse covering hundreds of square meters may result.

Whether within the ASCT or within distributary conduits, roofs over large void spaces that have been weakened likely collapse due the force of gravity, triggered by seismicity or the destabilizing motion of molten lava flowing around them (Figure 8). The roof breaks in isolated sections to produce skylight collapse, or over large areas to produce pervasive ASCT collapse. Roof talus accumulates

on the subsiding mass of lava below. In some cases, roof talus is overprinted by lava that occupies the void space later in that eruption or during a subsequent eruption. In other cases where there has been no subsequent overprinting, roof talus remains visible on the surface below the collapse feature. It is unlikely that roof talus is re-incorporated into the flow from which it originated since contact of the subsiding molten lava with seawater will form a protective crust through which roof talus cannot penetrate.

The abundance of catastrophically collapsed lava flows near and within the ASCT probably results from the antecedent topography proximal to the eruptive fissure. Eruptions that flood the ASCT can be highly effusive, but the flow volume can only be sustained for a finite duration before waning due to the limited size of the axial melt lens. This means inflated flows can be voluminous but ephemeral, leading to the formation of large expanses of roof material that are thin relative to their expanse and readily susceptible to cracking. If lava is erupted over the substrate in the ASCT, the area covered by the flow may be 10's – 1000's of meters wide. Water may be trapped beneath the flow and many lava pillars form to transport the heated water to the surface of the flow [*Gregg et al,* 2000], and eventually support roofs over void spaces (Figure 8). Eruptions that flood narrow distributary channels and travel far from the primary vent are not likely to produce areally expansive collapse features due the constriction of bounding walls and consequent roof support geometry. The likelihood of thick roofs supported by bounding walls far from the eruptive fissures suggests that

collapse features far from the eruptive fissure will be small in scale and less abundant than those seen at the ASCT.

2.3 Conclusions

The style and distribution of collapse features and flow morphologies at 9°37' N were mapped to produce a comprehensive database of volcanic terrain associated with the ridge offset. Lava drip structures and patinas observed on samples collected near collapse features during *Alvin* dives were analyzed to elucidate lava emplacement mechanisms and eruption processes, and yield working models for collapse genesis. Key findings of this research are:

(1) 13% of the total surface area surveyed at the ridge crest shows some degree of collapse.

(2) 89% of all collapse occurs in lobate lavas.

(3) Large collapse features, revealing void spaces 0.5-20 m deep, are more strongly associated with the ASCT than small collapse features which expose voids <50 cm deep.

(4) Small collapse features typically occur at the apex of smooth-surfaced lobes, have a sub-circular shape, and are <2 m in diameter.

(5) Many small collapse roof samples and some large collapse roof samples show lava drip structures and patinas.

(6) Lava drip structures and patinas can plausibly be explained by the existence of a vapor phase during lava emplacement. The vapor phase

would allow for thermal insulation of molten lava from the surrounding seawater, and thus allow drip structures to propagate while preventing cracking of the upper carapace of flows (Figures 7 and 8).

My results suggest that trapped vapor and antecedent topography are the primary controls on collapse formation at the 9°37' N ridge offset. Small collapse roofs are inferred to be thermally buffered by a vapor phase at some time during the eruption, as evidenced by the smooth surfaces of the lobes in which they form and the drip structures and oxidation residues on the underside of collapse roofs. Large collapse associated with deep and extensive void spaces occurs after lava drain-away from inflated lava flows. Vapor pockets associated with large inflated lava ponds may allow roofs to remain thin, thus focusing areas where collapse initiates.

If the surficial expression of collapse seen at the 9°37'N site is indicative of the existence of void spaces below the surface of the flow, porosities inferred by Vera et al. [1994] and Christeson et al. [1992] might be attributable to the presence of large-scale conduit systems plumbing the ridge crest, as well as remnant void spaces from previous eruptions. Subsurface void space is influenced by the tendency of lavas to infill pre-existing conduits and collapse features, but lobate lavas may conceal void spaces that are not collapsed. My model suggests that some percentage of the porosity seen in seismic reflection profiles is related to intact void spaces. Additional data from detailed gravity and

magnetic surveys and seismic reflection profiles could yield information about shallow subsurface structure that would better delineate the bounds of the porosity associated with the ASCT. Quantification of collapse would also prove useful to the modeling of hydrothermal systems and the transport and distribution of biological species living in these extreme environments.

CHAPTER 3: COMPARISON OF COLLAPSE DISTRIBUTION AND ABUNDANCE AT A MID-OCEAN RIDGE SEGMENT END AND CENTER 9°37'N AND 9°50'N

3.1 Comparative statistical analyses of flow morphologies and collapse features at 9°50'N and 9°37'N

The observations and analyses gathered from the 9°37'N ridge offset data are used in chapter 2 to develop conceptual models for the creation of void space in the upper few meters of oceanic crust, and the exposure of those void spaces via collapse. The data at 9°37' N form a densely sampled grid that allowed me to examine collapse processes at the scale of meters. In order to test the hypotheses put forward in chapter 2, I have subsequently conducted an identical analysis of the flow morphology and collapse features of the ridge crest at 9°50'N. The 9°50' N data set was collected to address different scientific questions, and therefore is not as densely sampled as the 9°37' N data set. Additionally, the character of the ridge crest is different based on sidescan imagery, bathymetric data, estimates of depth to the axial magma lens, and time since most recent volcanism. However, both sites have the same spreading rate, are morphotectonically defined as 4th order [*Haymon et al.*, 1993], and are part of the same second order segment. The juxtaposition of these sites at a segment center and a segment end make them an interesting case study in collapse style and

distribution relative to the ASCT. Thus, using the same methodology described in chapter 2, I analyzed the 9°50' N data to test and refine my model.

3.1.1 Morphology Types

Photographs showing morphology types at the 9°50'N segment center location have been analyzed and categorized based on volcanic morphologic types described in chapter 2 and originally defined by Ballard et al. [1979]. A comparison of the distribution of morphologic types at 9°50'N and 9°37'N shows that pillows are more abundant at 9°50'N, with 10% of all morphologies documented as pillows (versus 3% at 9°37'N) (Figure 9). However, sheet flows are more common at the 9°37' N site, with values for all sheet flows combined (sheet, hackly, and ropy) at 9°50'N being only 11% (versus 24% at 9°37'N). This result is surprising, given that low effective viscosity sheet flows and hydrothermal vents are both commonly associated with areas of active volcanism, yet the 9°50'N site is thought to have been more recently and frequently active than the 9°37'N site due to its location at the center of a segment. Morphologic types in the ASCT at 9°50'N are dominated by lobate flows, while at 9°37'N a greater proportion of ASCT lavas is made up of hackly sheet flows (Figures 2 and 3).

3.1.2 Collapse Features

Collapse features at the 9°50'N and 9°37'N site have been compared for distribution relative to the ASCT, and the abundance of each collapse type over the spectrum of collapse styles described in chapter 2. We used F and Student's t tests to evaluate the similarity of collapse population distributions relative to the ASCT, and at both the 9°37'N and 9°50'N sites small collapse distributions have significantly different variances than large collapse distributions at the 99% confidence level, though the two populations have the same means. This analysis bolsters the conceptual model developed in chapter 2, by showing that although collapse style abundances along the ridge crest may peak in the same location relative to the ASCT, small collapse is almost evenly distributed throughout the ridge crest area, while large collapse clusters near the ASCT. My model predicts that close to the axis, a well-developed network of tubes, channels, or fissures (including the bounding walls of the ASCT), confines voluminous flows and causes them to inflate *in situ*, yielding large collapse features. At more distal locations, the antecedent topography of the ridge crest has been infilled by lava, causing flows that persist off axis to spread out in thin layers and bifurcate. These thin and sluggish flows are much less likely to inflate than those near axis, so the resulting collapse features tend to be shallow and have small diameters in plan view, typical of small collapse.

There is a striking difference in the abundance of each collapse type at 9°50'N and 9°37'N (Figures 10 and 11). At the 9°50'N site, 56% of all documented collapse is small collapse, as compared to only 19% at the 9°37'N

site. Accordingly, only 44% of the collapse at the 9°50'N site falls under the category of large collapse, with 28% pervasive, 9% roofs, 5% skylights, 1% bridges, and <1% multi-story collapse. The 9°50' N collapse style distribution is highly bi-modal, between small collapse and the largest collapses that are most commonly associated with the ASCT. This is in contrast to the more even distribution of collapse styles at the 9°37' N site (small: 19%, skylight: 29%, bridge: 4%, roof: 30%, pervasive: 17%, multi-story: >1%). In an attempt to quantify these differences and their relevance to ridge processes, I have mapped the distribution of collapsed area relative to the ridge crest at both 9°37'N and 9°50'N.

The 9°37'N and 9°50'N sites were sampled at different frequencies by the WHOI-TCS and *Alvin*. The 9°37'N ridge offset survey sampled lines both perpendicular and parallel to the ridge crest, while the 9°50'N site was only sampled in the along-axis direction. In addition, 60% of the tows at the 9°50'N site were run in the ASCT, while only 20% of the tows at the 9°37'N ridge offset were run in the ASCT. There is a marked morphotectonic difference between the two sites in that the 9°50'N site has only one ASCT, while the 9°37'N ridge offset has two overlapping ASCTs. In an initial analysis aimed at elucidating large-scale ridge segment properties, I have included all the data from both the 9°37'N and 9°50'N sites, but weighted the values for ASCT collapse to reflect the heavier sampling of the 9°50'N ASCT. This weighting was accomplished by multiplying the values for the 9°50'N ASCT data by a scaling constant to equalize the

percentage of the total survey data within the ASCT between the two sites. Area values have been calculated for each site, with the result that at the 9°37'N site, 13% of the total surface area surveyed shows collapse, while at the 9°50'N site 12% of the surface area is collapsed. This result is surprising given that collapse styles and distributions are very different at the two sites. Area values have been binned in 100 m intervals moving away from the ridge axis perpendicularly out to 900 m (Figure 12). The resultant histograms show a peak of collapse centered in the ASCT at 9°50'N, with a much broader collapse signal out to ~300m on either side of the two ASCTs at 9°37'N. These collapse signatures are consistent with the morphology of the ASCT at the two locations. At 9°50'N, the ASCT measures only 40-70 m wide [*Haymon et al*, 1993], while at 9°37'N it measures from 20-280 m wide over the length of the ridge offset. Barone et al. [1988] propose that volcanic and tectonic features of a plate boundary segment narrow at the segment center, and broaden and deepen at the segment ends due to the temperature dependence of crustal rheology. My analyses are consistent with this interpretation at both the micro level of collapse size, and the macro level of collapse distribution. These results imply that large collapse features may be indicative of a lack of recent volcanism, and the infilling of antecedent collapsed void spaces associated with active volcanism. Conceptually, the relatively flat distribution of collapse type abundances previously noted at the 9°37'N ridge offset is reflective of the increased number of collapsed lava ponds, tubes, and lobes at all scales in the collapse-rich zone between the two limbs of the ridge offset.

In a second comparative analysis, I have isolated each limb of the ridge offset at 9°37'N and compared them individually and stacked to the collapse area distributions at 9°50'N (Figure 13) in an attempt to factor out the effect of a second ASCT on the collapse analysis. To do this I subtracted all data 150 m to the west of the eastern limb of the ASCT, and 150 m to the east of the western limb of the ASCT, to isolate the data associated with each individual limb of the overlapping ridge offset. The broad signature of collapse at 9°37'N is damped by the removal of the second ASCT, however the collapse signature is still wider than at 9°50'N. Additionally, the curves from the east and west limbs of the 9°37'N ridge offset differ, with collapse areas along the western limb of the ASCT peaking 100 m off axis as opposed to in the ASCT. Based on the hypothesis that the eastern limb of the ASCT is actively propagating south, I infer that the off-axis peak in collapse on the western limb of the ASCT could be the result of volcanic overprinting of collapse by the propagating limb.

A final comparison further constrains the data at 9°50'N and 9°37'N to two boxes measuring ~1850 m in length and 600 m in width centered over the ASCTs at 9°50'N and 9°37'N (Figures 2 and 3). I have stripped out all ASCT data and *Alvin* dive data, and scaled the counts to make the analyses as comparable as possible with the available datasets. The 9°50'N data box contains 3 survey lines covering a total of 0.4% of the survey box area, while the 9°37'N data contains data from ~5 lines, for a total areal coverage of 0.7% of the survey box. The different line spacing relative to the ASCT at the two sites affects the

resultant areal distribution curves in predictable ways, but the gross patterns of broad collapse areas at 9°37'N persist even when measurable ridge overlap effects have been removed from the picture, consistent with Barone et al.'s [1988] "hourglass" model (Figure 14).

There is a bimodal distribution of collapse area maxima in all analyses of the 9°50'N site, regardless of scale (Figures 12, 13 and 14). The areal distributions calculated for collapse progressing away from the ridge crest are the sums of all sizes of collapse occurring within a given distance from the ASCT. However, I infer that the collapse area maxima observed may be the areal expression of the small and large collapse bimodality previously noted for collapse style abundances at this location. Zones of collapse at the 9°50'N site are concentrated within the ASCT and in an area parallel to the ASCT between 100-200 m away from the axis. One hypothesis is that a transect across the ridge axis out to the maximum lava flow transport distance from the ridge crest represents a snapshot of ridge development and lava emplacement mechanisms through time. If I invoke this hypothesis and view the ridge crest transect as a single unit in time, based on the models for collapse formation developed in chapter 2, large collapse may dominate the collapse regime within the axial eruptive fissure, while a secondary network of smaller tube and lobe collapse dominates the topography in a zone 100-200 m off axis. Conceptually, flows that are limited in volume may be confined to the ASCT, with occasional voluminous episodes overflowing the ASCT bounding walls and terminating at 100-200 m

from the axis. Alternatively, local, off-axis ridge-parallel eruptions may create collapse features at the observed distance from the ridge crest.

An alternative explanation to the "ridge snapshot" view described above is that the expression of collapse currently noted in the ASCT is preserved in the spreading seafloor over time. As seafloor is rafted away from the ASCT, the seafloor collapse signature records periods of high eruptive activity or quiescence at the ridge crest. In this scenario, the zone of collapse 100-200 m off axis may be indicative of a volcanically active period along this portion of the ridge crest at some time in the past. The zone between 100-200 m would then be separated from the current ridge crest by a zone representing a quiescent period in ridge volcanism. Dampening of the collapse signature off axis may be attributable to infilling of collapse features by a combination of subsequent lava flows and sediments. This second alternative seems less likely, due to the fact that collapse signatures would tend to get overprinted with time as seafloor is rafted away from the ridge crest. Many flows have been observed to travel several hundreds of meters off axis, and it is unlikely that intact collapse features would persist through subsequent eruptive periods, particularly in areas of frequently active volcanism, due to infilling of void spaces by subsequent flows.

3.2 Conclusions

Statistical analyses of the areal distribution of collapse, and its co-occurrence with distinct morphologic characteristics of the ASCT, have allowed me to examine collapse over a range of volcanic features along the ridge crest.

The detailed conceptual models for void space creation and collapse initiation developed in chapter 2 have helped to explain the spatial distribution of collapse at two morphologically and volcanically disparate locations along the same fast-spreading ridge crest. Key findings of this research are:

(1) 12-13% of the total surface area surveyed at the ridge crest shows some degree of collapse, regardless of ASCT morphology and state of active volcanism.

(2) The 9°50'N segment center is dominated by small collapse and the 9°37'N segment end is dominated by large collapse.

(3) The 9°50'N segment center shows a bi-modal distribution of small and large collapse, which is strongly correlated with a bi-modal distribution of ASCT and off-axis collapse.

(4) The 9°37'N ridge offset shows a tapering distribution of large to small collapse, and a broad swell of collapse features proximal to the ridge axis.

(5) The 9°37'N ridge offset has more sheet flows both in and proximal to the axis than the 9°50'N segment center.

My results suggest that the type of collapse within a kilometer of the ridge axis in two locations along the fast-spreading EPR is reflective of volcanic processes within the ASCT, and the thermal regime plumbing the ridge crest. The ASCT at the recently active 9°50'N site is only 40-70 m wide, and the areal distribution of collapse at this location clusters tightly within the ASCT. The

ASCT at 9°37'N is complicated by two ASCTs in an overlapping relationship, and as a consequence the areal distribution of collapse in this location is broadly distributed in a zone extending between the two limbs of the ridge offset. Discrepancies in collapse size and areal distribution at the two sites may be the result of relative age and frequency of active volcanism, which in turn results from ridge segmentation patterns related to the depth of the axial melt lens below the ridge crest.

APPENDIX A: Table

Table 1. COLLAPSE CHARACTERISTICS

collapse type	depth	areal extent of individual collapses	roof thickness	proximity to axis	source of void space below collapse
small	5 mm - <0.5 m	cms - 2 m	1 mm - <2 cm	ms - >250 m	inflated lobate toe
skylight	5 cm - <1 m	1 - 2 m	5 mm - >5 cm	ms - >250 m	inflated lobate toe or small lava tube
bridge	10 cm - <2 m	ms - >4 m	1 - 10 cm	ms - 100 m	group of inflated lobes or large lava tube
roof	10 cm - >4 m	ms - 10s ms	1 - 10 cm	ms - 100 m	group of inflated lobes or large lava tube
pervasive	1 m+	ms - 10s ms	1 - 10 cm	in axis or ms away	inflated lava pond
multi-layer	1 - 5 m	ms	1 cm - >2 m	in axis or ms away	inflated lava pond or large lava tube

APPENDIX B: Figures

Figure Captions

Figure 1:

Map showing location of study areas relative to major plate boundaries and continental landmasses. The Clipperton and Siqueiros Transforms, which offset the East Pacific Rise, are indicated.

Figure 2:

On left half of figure, map showing DSL-120 sidescan data between 9°35'N and 9°39'N, collected during the AHA-Nemo2 cruise. Sidescan swaths measure ~1km in width. The ASCT can be traced trending N-S, with the ridge offset centered at 9°37'N. Note the prominent pillow ridges to the east of the ASCT, and the large collapsed channel trending east off-axis from the ridge offset. On right half of figure, map showing morphologic data from *Alvin* and the WHOI-TCS between 9°36'N and 9°38'N, collected during the ALGRAV2000 cruise. Data trending N-S are WHOI-TCS digital still image data, and data trending E-W are *Alvin* video still frame data. Lobate morphologies are red, sheet morphologies are green, pillow morphologies are blue, and the ASCT is shown in black and was digitized from ArgoII 1989 visual and acoustic data. Note the linear alignment of pillow ridges to the east of the ASCT. Sheet flows are concentrated within the ASCT, and around the base of the eastern (propagating) limb of the ridge offset. The survey box used in the statistical analyses of chapter 3 is outlined in blue.

Figure 3:

On left half of figure, map showing DSL-120 sidescan data between 9°45'N and 9°54'N, collected during the AHA-Nemo2 cruise. Sidescan swaths measure ~1km in width. The ASCT can be traced trending N-S. On right half of figure, map showing morphologic data from the WHOI-TCS between 9°45'N and 9°54'N. Lobate morphologies are red, sheet morphologies are green, pillow morphologies are blue, and the ASCT is shown in black and was digitized from ArgoII 1989 visual and acoustic data. The survey box used in the statistical analyses of chapter 3 is outlined in blue.

Figure 4:

Left panel shows DSL-120 sidescan map of the 9°37'N ridge offset site, overlain with data showing the location of small collapse in blue. Location of the ArgoII 1989 digitized ASCT is seen in white. Note the random distribution of small collapse throughout the survey area. Right panel shows the same site, overlain with data showing the location of large collapse in red, ASCT in white. Large collapses cluster preferentially close the ASCT and ridge offset.

Figure 5:

Photographs showing examples of common collapse types observed at the 9°37'N ridge offset site. Image descriptions from left to right and top to bottom of figure. (a) 6m x 4m. Plan view of small collapse confined within individual lobate lobe. Note the glassy, uncracked surface of the remnant lobate. (b) 1m x 1m Side

view of small collapse through crust measuring ~2cm in thickness. (c) 6m x 4m Plan view of bridge collapse punctured by skylight collapses. It is easy to imagine from this photograph the progression from smaller to larger collapse features through time. Depth of void space ~1m. (d) 2m x 2m Side view of skylight penetrating large lobate lobe. Crust of roof does not appear to be very thick at this location. (e) 6m x 4m Plan view of multi-layered roof collapse. Void space ~2m in depth. (f) 4m x 2m Side view of roof collapse through very thick roof crust, at least 10cm thick. Note layering of roof crust, and talus at the base of the roof. (g) 6m x 4m Plan view of multi-story collapse. In this instance, collapse feature is made of two nested skylights. Collapse surfaces are separated by ~0.5m, and the total void space is ~3m deep. (h) 6m x 4m Plan view of pervasive collapse showing two remnant lava pillars capped by lobate crusts. Depth of void space ~3m. Note talus accumulation at base of collapse.

Figure 6:

Photographs showing the variety of physical features and structures commonly observed on the underside lava flows that exhibit evidence of interaction with a vapor phase. Descriptions from left to right and top to bottom of figure. (a) 0.2m x 0.15m Underside of a lobate crust (sample 2357-1) from collapsed roof of ASCT. Sample is ~2 cm thick with a microvesicular "frothy" surface texture and has cuspate and drip structures up to 2cm in length. Note the runny lava textures preserved in the drip structures that suggest the molten lava was not quenched immediately upon eruption. (b) 0.2m x 0.15m 5 cm-thick lava fragment (2497-6)

from roof of collapse showing drip structures up to 2cm in length. The thickness of this flow is more than twice that shown in photograph (a). Note the more massive interior, cooling fractures, and vesicular zone along the underside of the flow. (c) 0.1m x 0.07m Fragment of top of a lava pillar (2354-V) with large cuspate structures that appear to be walls of lava bubbles. The interior surfaces have a shiny, oxidation patina. (d) 0.2m x 0.15m Jumbled sheet flow (2759-7) containing a 3cm diameter "pipe vesicle" or bubble. At least one of these bubbles appeared to be unbroken upon recovery and contained water.

Figure 7:

Schematic representation of the formation of small collapse in lobate lavas. Each panel measures ~2m by 6m. Top panel shows molten lava (red) being extruded across a porous and permeable substrate infiltrated by seawater (black). The reaction of molten lava with seawater immediately produces a vapor phase (yellow), as seawater heated past the critical point is flashed to steam. This thin layer of vapor insulates the upper cooled surface of the flow and prevents thermal stresses from cracking the lobate carapace. The middle panel shows the same lava flow at some later time during the eruption. Water trapped in the substrate has been channeled up through the body of the flow and trapped below the upper carapace where it fills a void space. Molten lava on the underside of the carapace drips into the heated void space to produce characteristic drip structures found on the underside of collapse roofs. The bottom panel shows the same lava flow after cooling and lowering of the molten lava at the core of the flow. Void spaces have

been infilled by water, and some roofs have been breached at their apex, exposing the voids below.

Figure 8:

Schematic representation of the formation of large collapse in a lobate flow. Each panel measures ~ 10m by 30m. In the top panel, molten lava (red) extruded across a porous and permeable substrate (black) that is infiltrated by seawater reacts with water to form a vapor phase. As in Figure 7, this vapor phase is preferentially channeled to the upper part of the flow where it is trapped by the cooled carapace. In this setting, lava is confined by antecedent topography and the vent source is inferred to be proximal to the location of the flow. In the middle panel, ponded lava begins to inflate, and continued water channelization through the flow produces characteristic lava pillars as the molten interior of the flow is chilled and solidifies around water pathways. Vapor pockets persist at the top of the flow, allowing drip structures to form, and preventing the crust above them from cooling and solidifying as quickly as the surrounding carapace. In the bottom panel, lava drain-away empties the flow carapace, leaving a cavernous void space highly susceptible to collapse due to its unstable roof geometry. Vapor pockets may act as the locus of collapse, or entire roof sections may fail due to the force of gravity triggered by seismicity or other local perturbations, if not supported from below by pillars or bounding walls.

Figure 9:

Histogram showing the relative abundance of flow morphology types catalogued at the 9°37'N ridge offset and the 9°50'N segment center.

Figure 10:

Histogram showing the relative abundance of collapse types catalogued at the 9°37'N ridge offset and the 9°50'N segment center. Note that the 9°37' N data re more evenly distributed than the bimodal 9°50' N data.

Figure 11:

Left panel shows DSL-120 sidescan map of the 9°50'N segment center site, overlain with data showing the location of small collapse in blue. Location of the ArgoII 1989 digitized ASCT is seen in white. Note the random distribution of small collapse throughout the survey area. Right panel shows the same site, overlain with data showing the location of large collapse in red, ASCT in white. Large collapses cluster preferentially close the ASCT.

Figure 12:

Top panel shows the distribution of all collapse at the 9°50'N segment center site out to 700m from the ridge axis. Bottom panel shows same distribution for the 9°37'N ridge offset site. The data within the ASCT have been normalized to minimize the effects of different sampling techniques between the two locations.

Figure 13:

Top panel shows distribution of all collapse at the 9°50'N segment center out to 700m off axis. Middle and bottom panels show same distributions for data from the west and east limbs of the 9°37'N ridge offset.

Figure 14:

Top panel shows distribution of collapse in survey box at the 9°50'N segment center out to 466m off axis. Bottom panel shows same distribution for data at the 9°37'N ridge offset. Distributions are affected by the small number of survey lines used in this analysis, yet the broad patterns observed in Figures 12 and 13 persist.

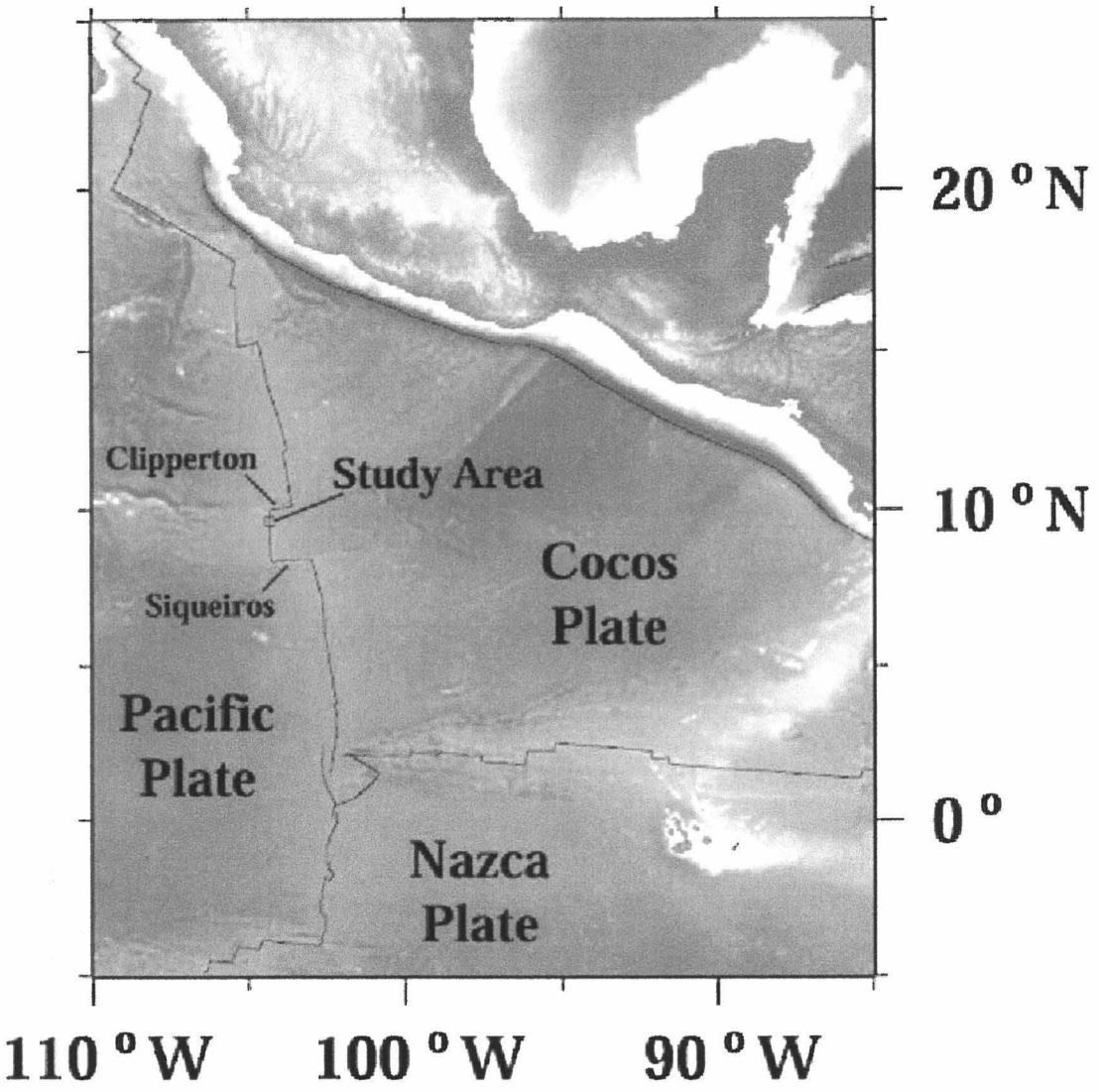
20 °N
10 °N
0 °
110 °W
100 °W
90 °W
Clipperton
Study Area
Siqueiros
Cocos
Plate
Pacific
Plate
Nazca
Plate

Figure 1

Figure 2

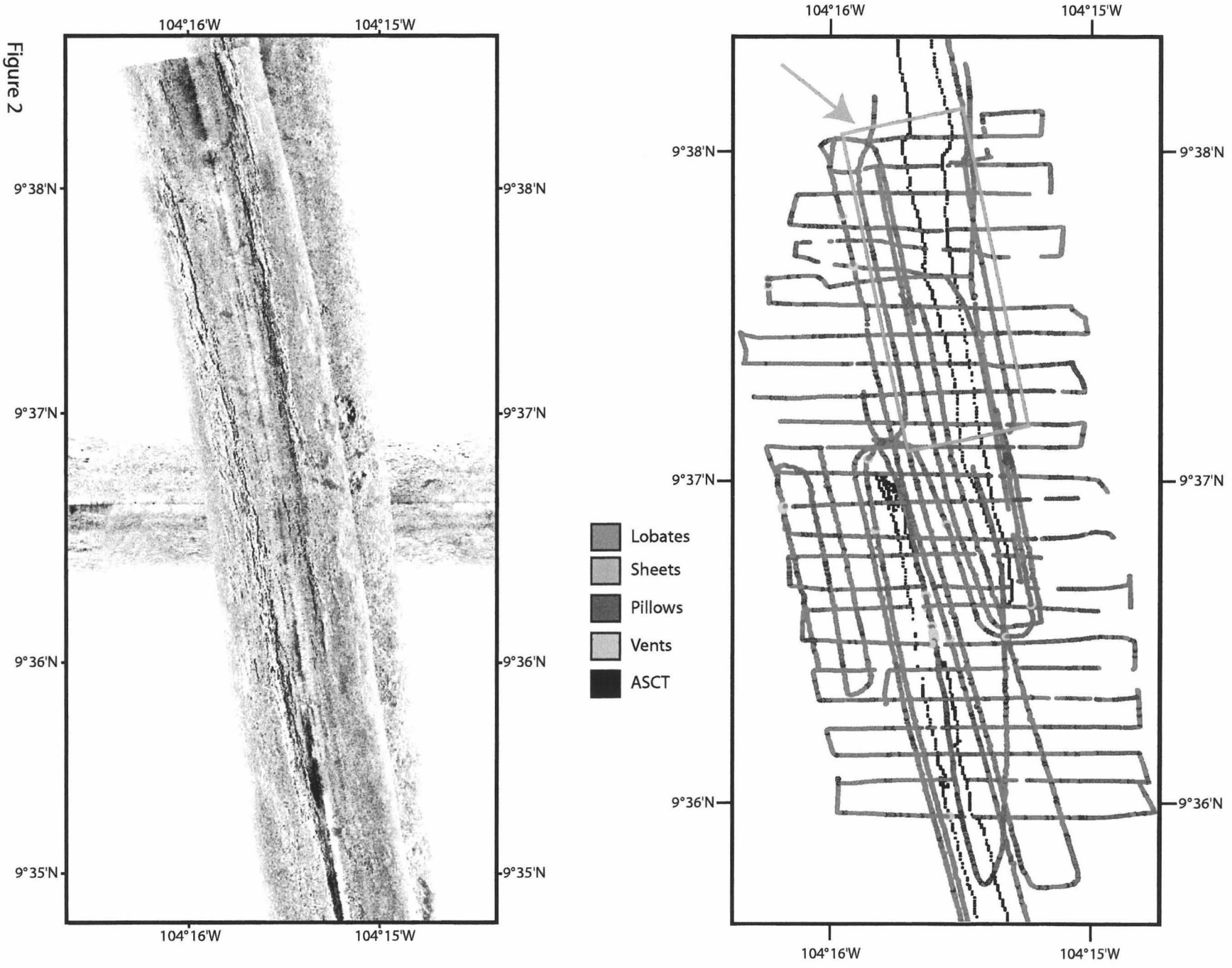
104°16'W
104°15'W
9°38'N
9°37'N
9°36'N
9°35'N
Lobates
Sheets
Pillows
Vents
ASCT

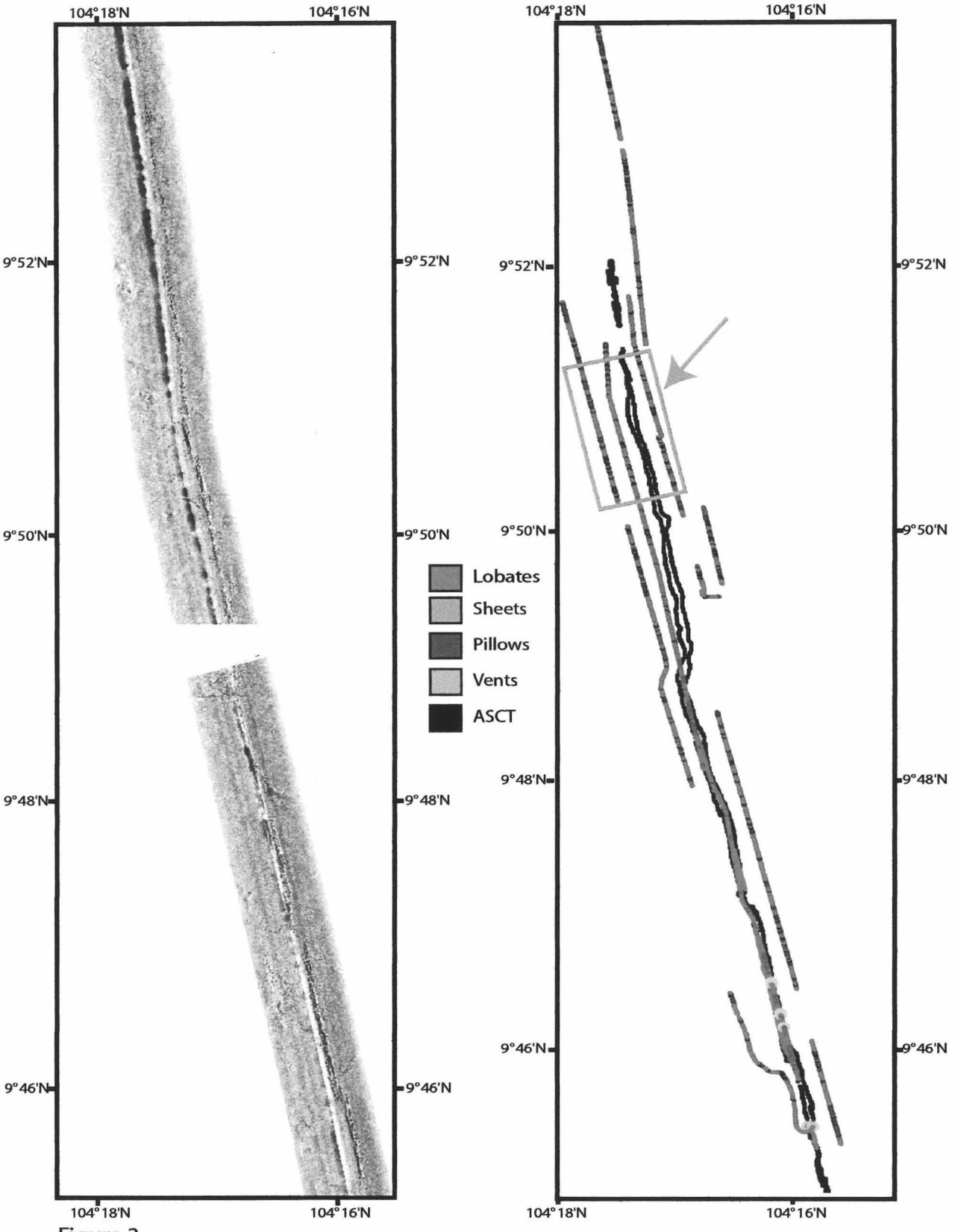
104°18'N
104°16'N
9°52'N
9°50'N
9°48'N
9°46'N
Lobates
Sheets
Pillows
Vents
ASCT

Figure 3

Figure 4

9°38'N
9°37'N
9°36'N
1.0km
0.5km
0.0km
104°16'W
Small Collapse
ASCT
104°15'W
104°16'W
Large Collapse
ASCT
104°15'W

Plan View - Towed Camera Photos

Side View - Alvin Photos

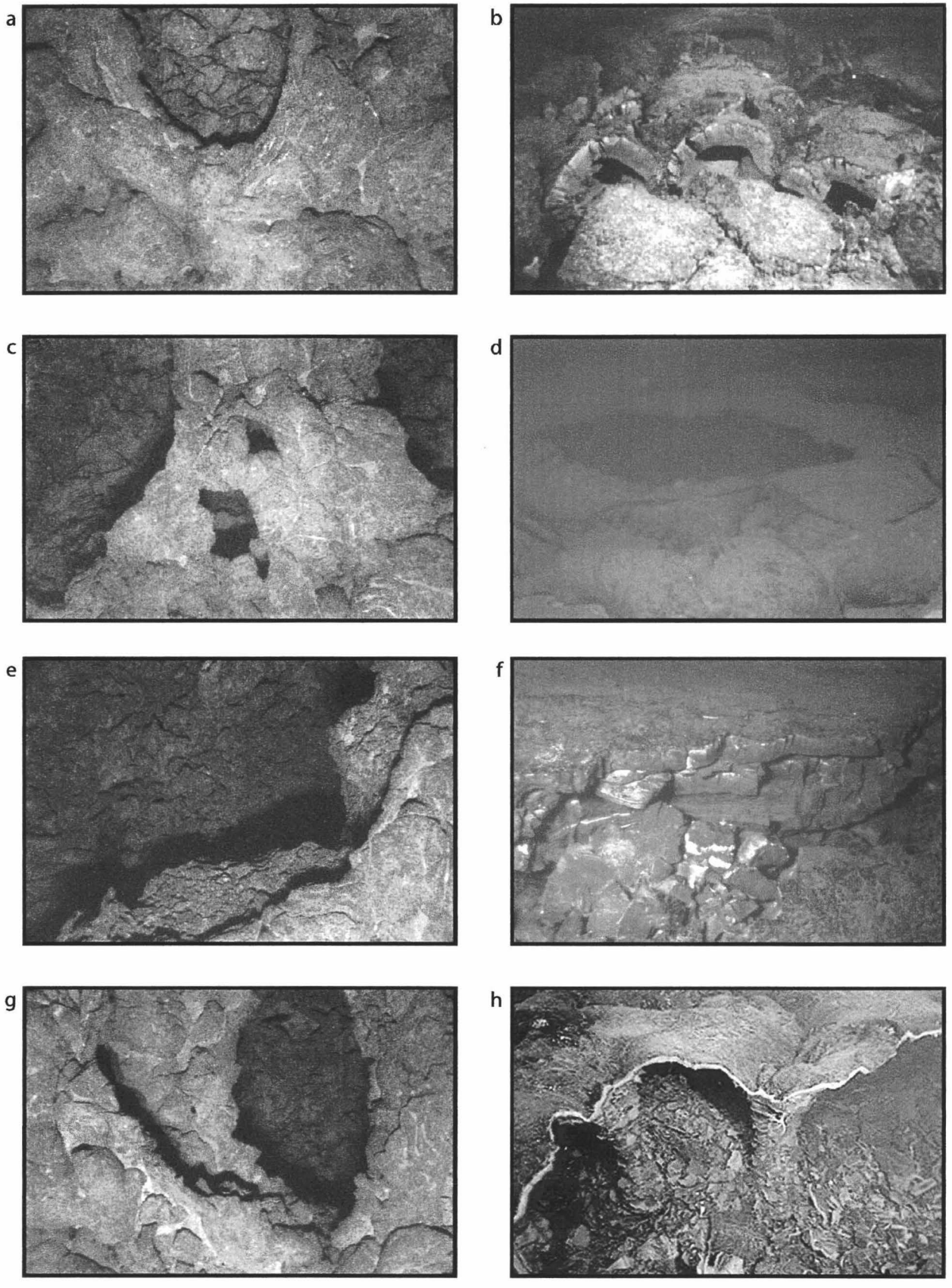

Figure 5

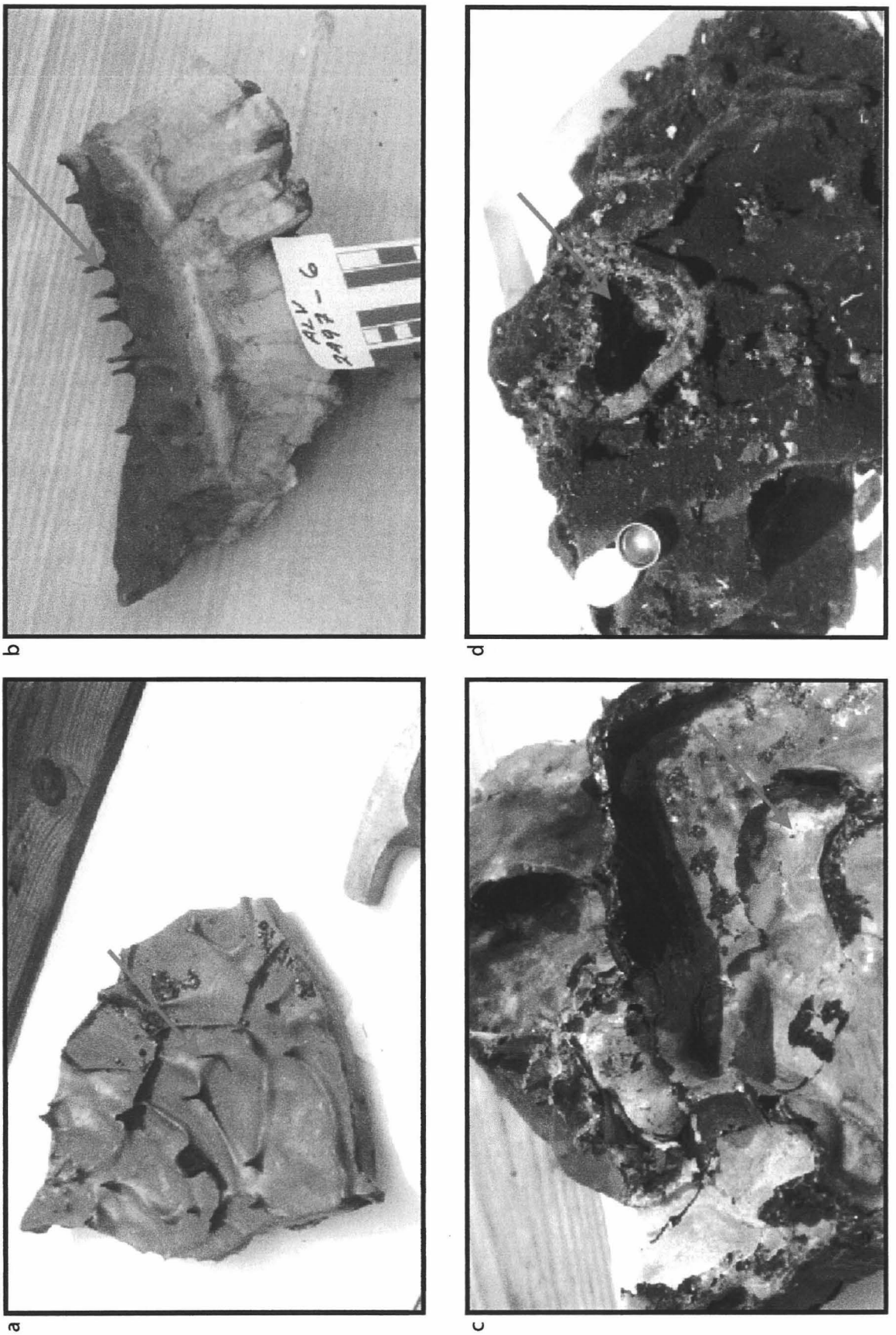

Figure 6

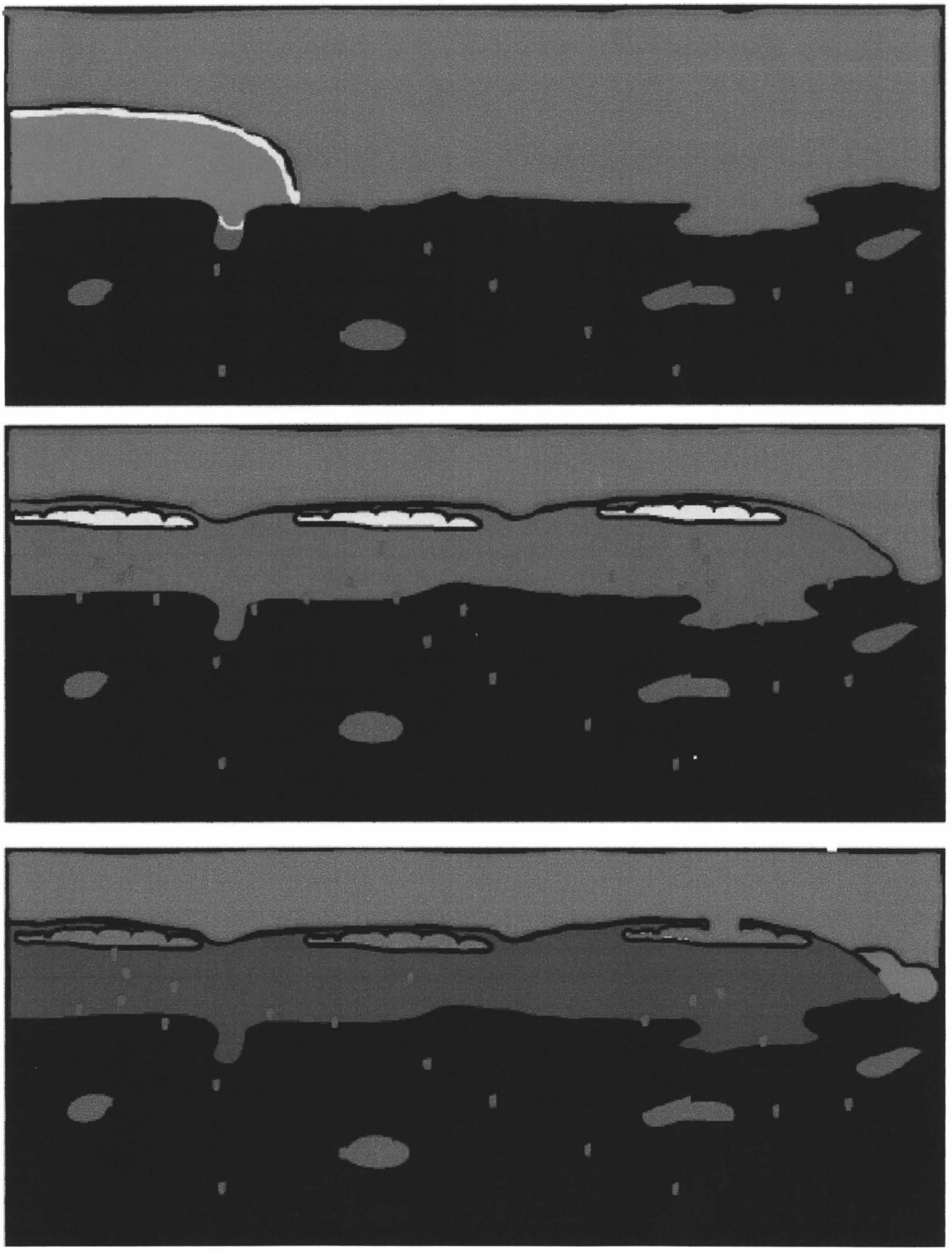

Figure 7

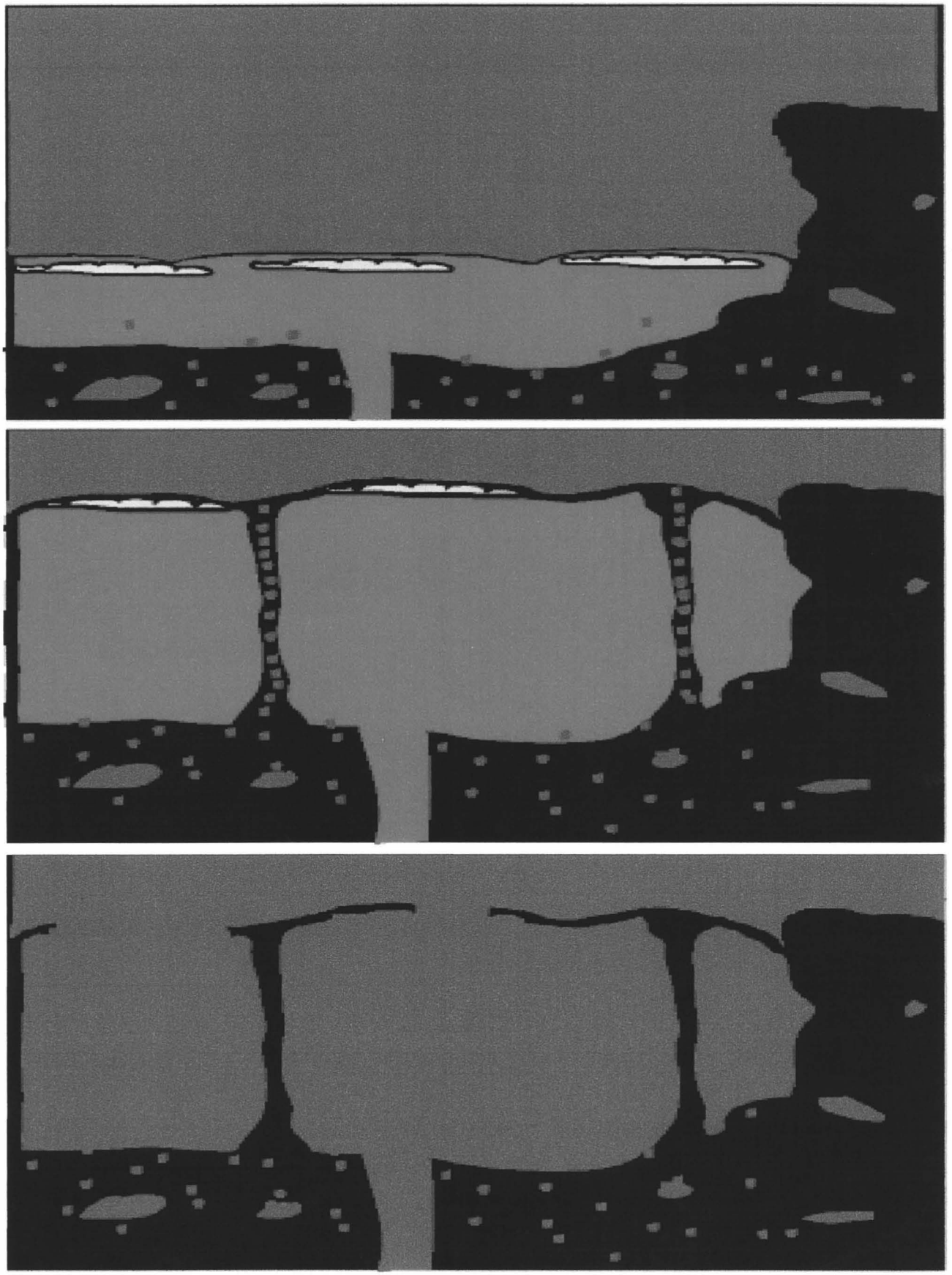

Figure 8

Figure 9

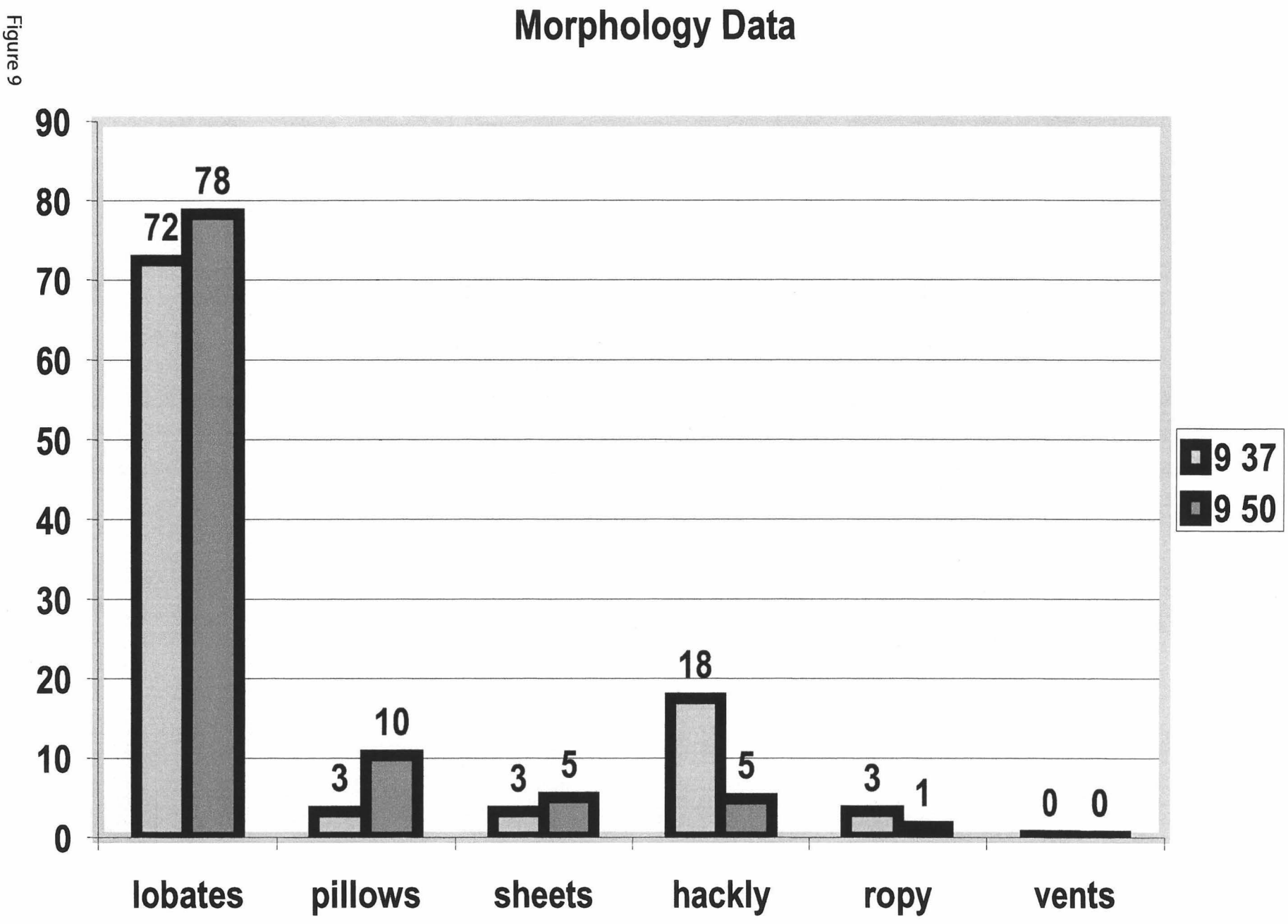
Morphology Data
90
80
70
60
50
40
30
20
10
0
72
78
3
10
3
5
18
5
3
1
0
0
lobates
pillows
sheets
hackly
ropy
vents
9 37
9 50

60

Figure 10

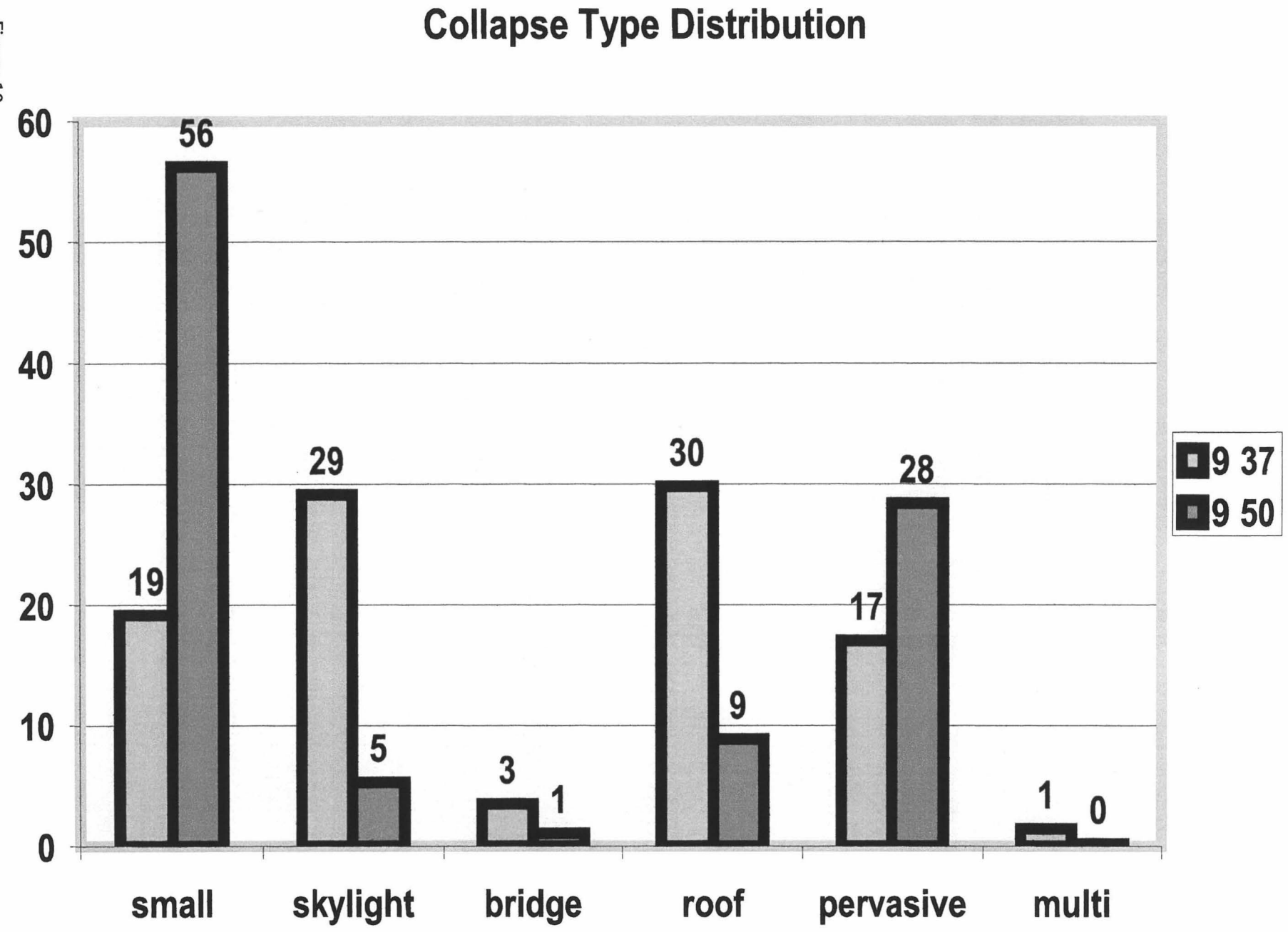
Collapse Type Distribution
60
50
40
30
20
10
0
56
19
29
5
3
1
30
9
28
17
1
0
small
skylight
bridge
roof
pervasive
multi
9 37
9 50

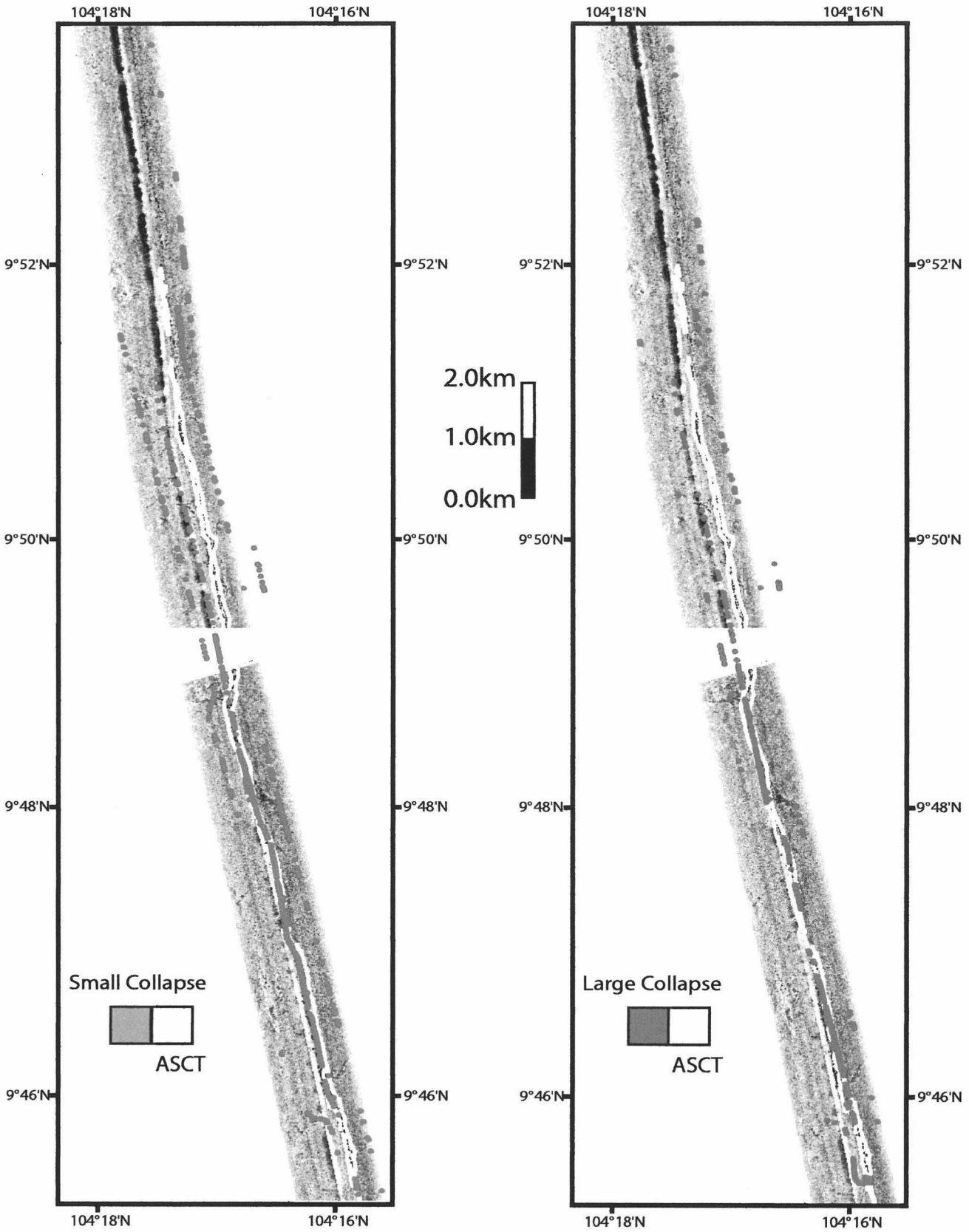
104°18'N
104°16'N
9°52'N
9°50'N
9°48'N
9°46'N
2.0km
1.0km
0.0km
Small Collapse
ASCT
Large Collapse
ASCT

Figure 11

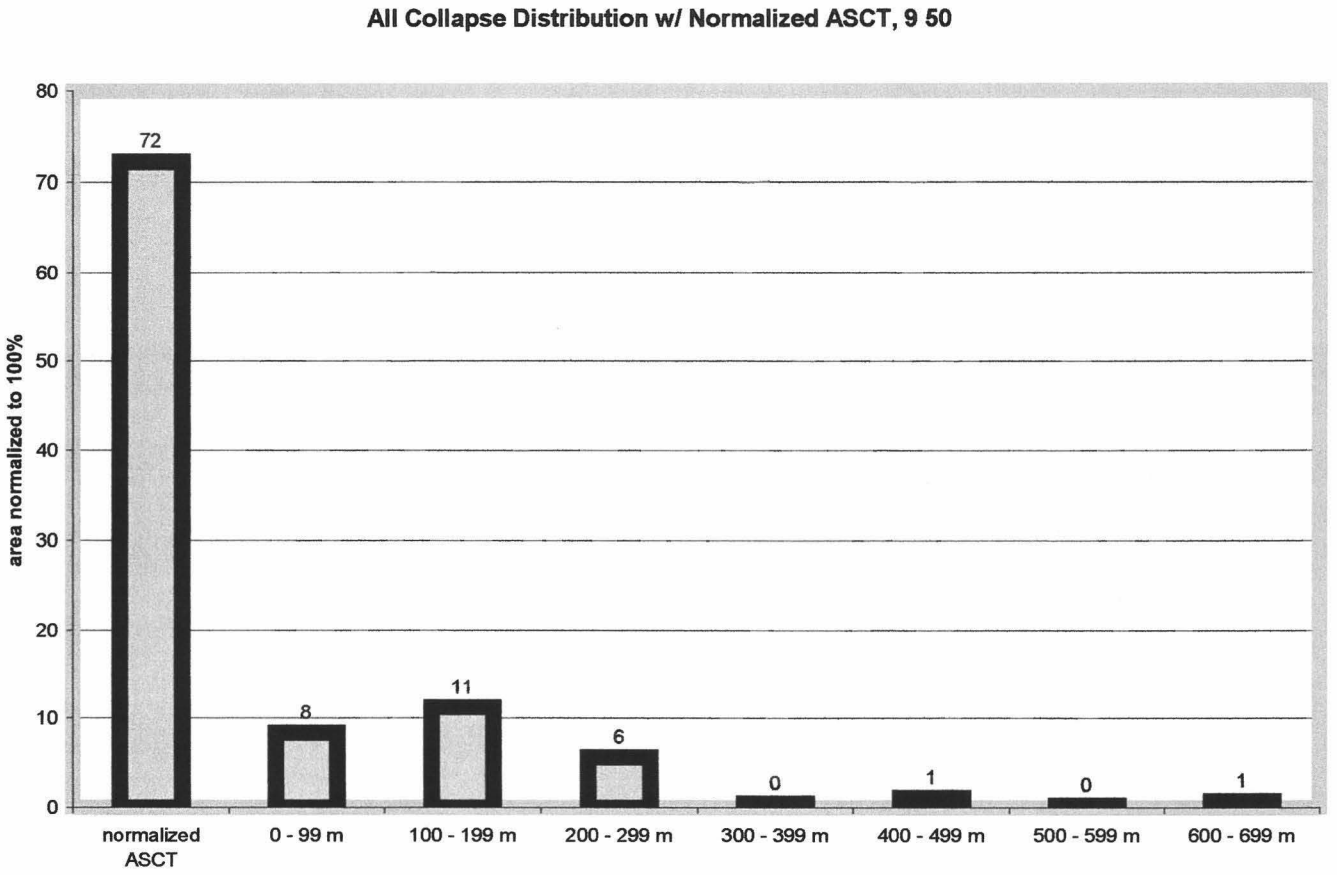
All Collapse Distribution w/ Normalized ASCT, 9 50
area normalized to 100%
80
70
60
50
40
30
20
10
0
72
8
11
6
0
1
0
1
normalized ASCT
0 - 99 m
100 - 199 m
200 - 299 m
300 - 399 m
400 - 499 m
500 - 599 m
600 - 699 m

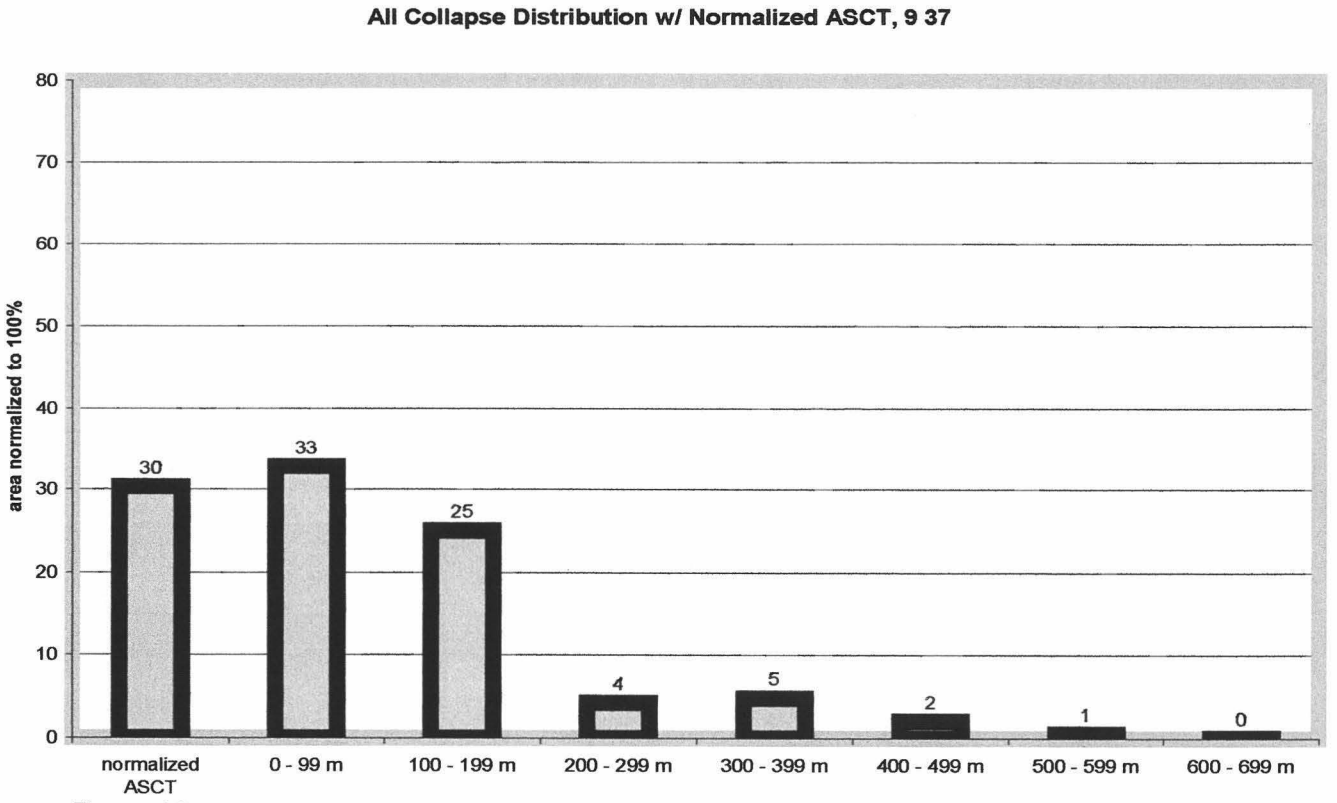
All Collapse Distribution w/ Normalized ASCT, 9 37
area normalized to 100%
80
70
60
50
40
30
20
10
0
30
33
25
4
5
2
1
0
normalized ASCT
0 - 99 m
100 - 199 m
200 - 299 m
300 - 399 m
400 - 499 m
500 - 599 m
600 - 699 m

Figure 12

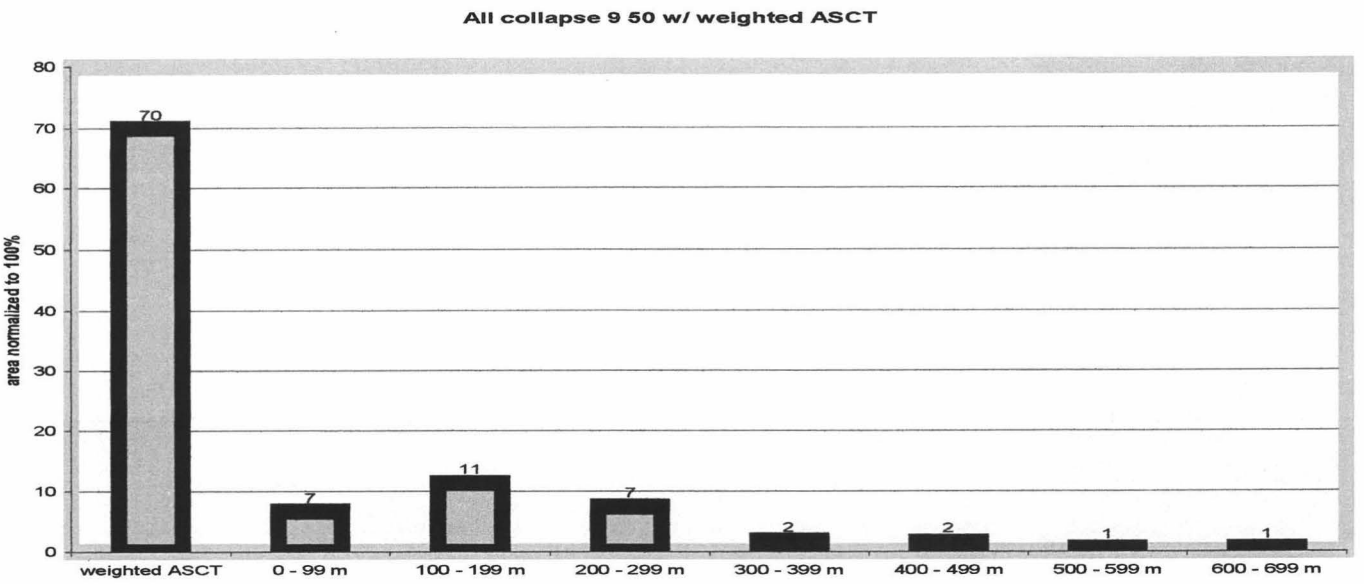
All collapse 9 50 w/ weighted ASCT
area normalized to 100%
80
70
60
50
40
30
20
10
0
70
7
11
7
2
2
1
1
weighted ASCT
0 - 99 m
100 - 199 m
200 - 299 m
300 - 399 m
400 - 499 m
500 - 599 m
600 - 699 m

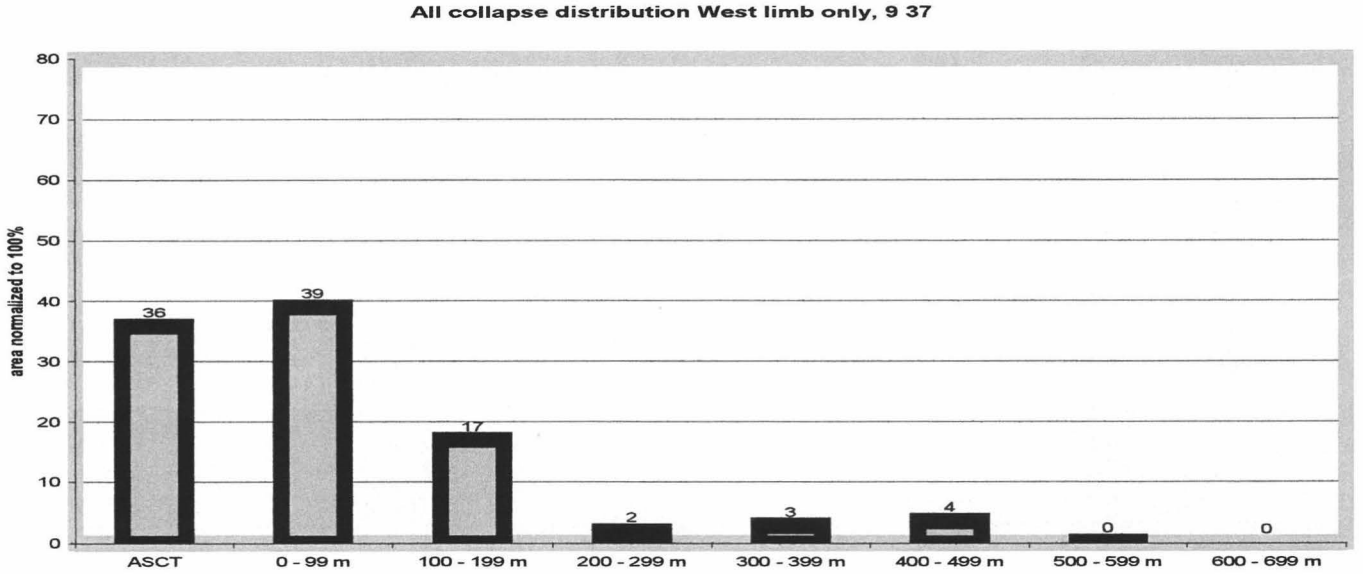
All collapse distribution West limb only, 9 37
area normalized to 100%
80
70
60
50
40
30
20
10
0
36
39
17
2
3
4
0
0
ASCT
0 - 99 m
100 - 199 m
200 - 299 m
300 - 399 m
400 - 499 m
500 - 599 m
600 - 699 m

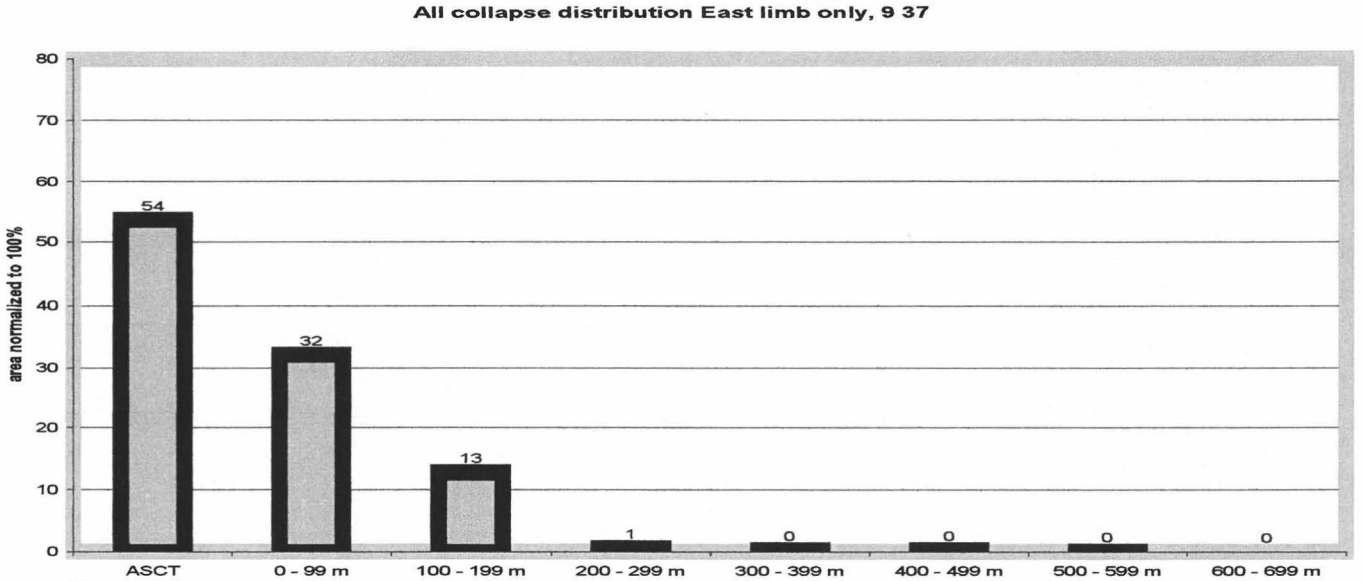
All collapse distribution East limb only, 9 37
area normalized to 100%
80
70
60
50
40
30
20
10
0
54
32
13
1
0
0
0
0
ASCT
0 - 99 m
100 - 199 m
200 - 299 m
300 - 399 m
400 - 499 m
500 - 599 m
600 - 699 m

Figure 13

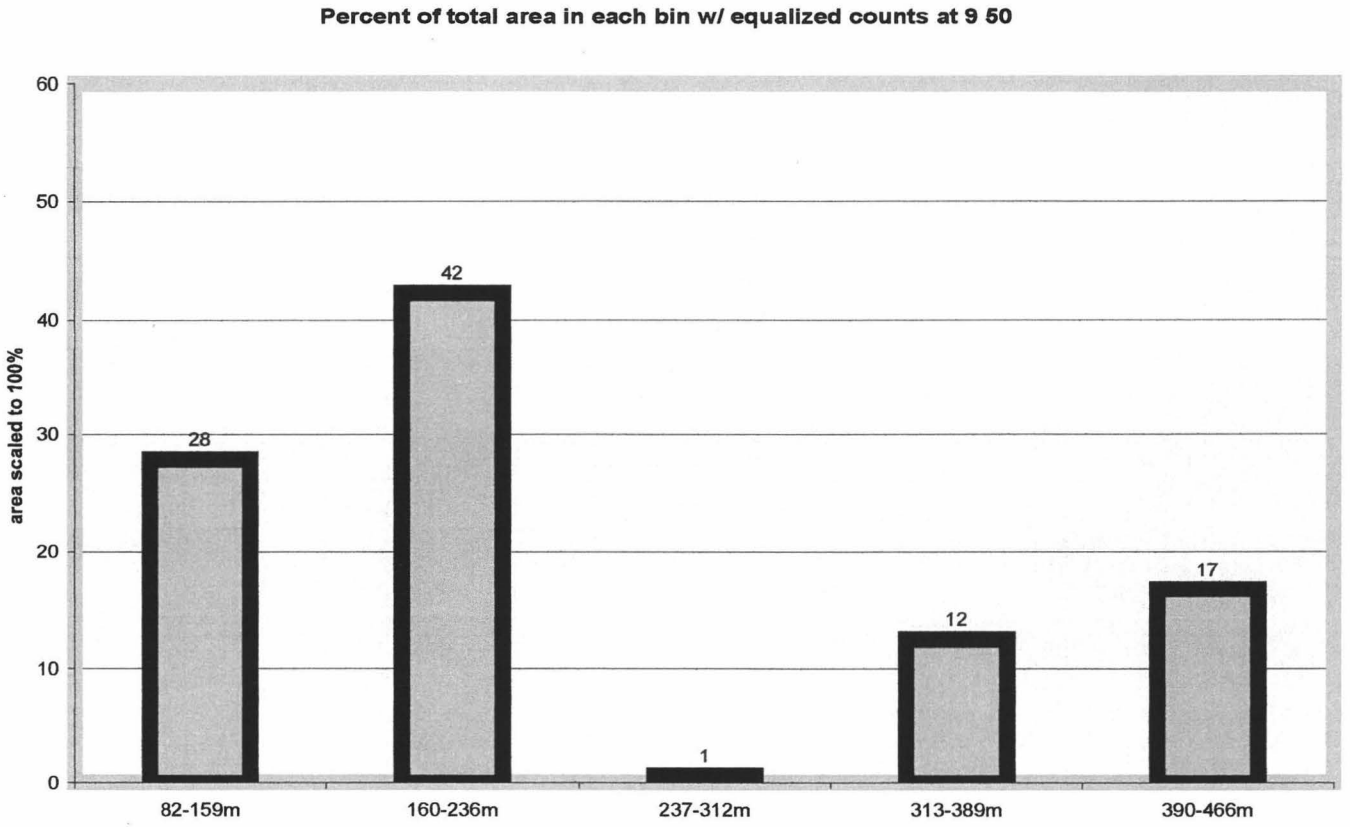
Percent of total area in each bin w/ equalized counts at 9 50
area scaled to 100%
60
50
40
30
20
10
0
28
42
1
12
17
82-159m
160-236m
237-312m
313-389m
390-466m

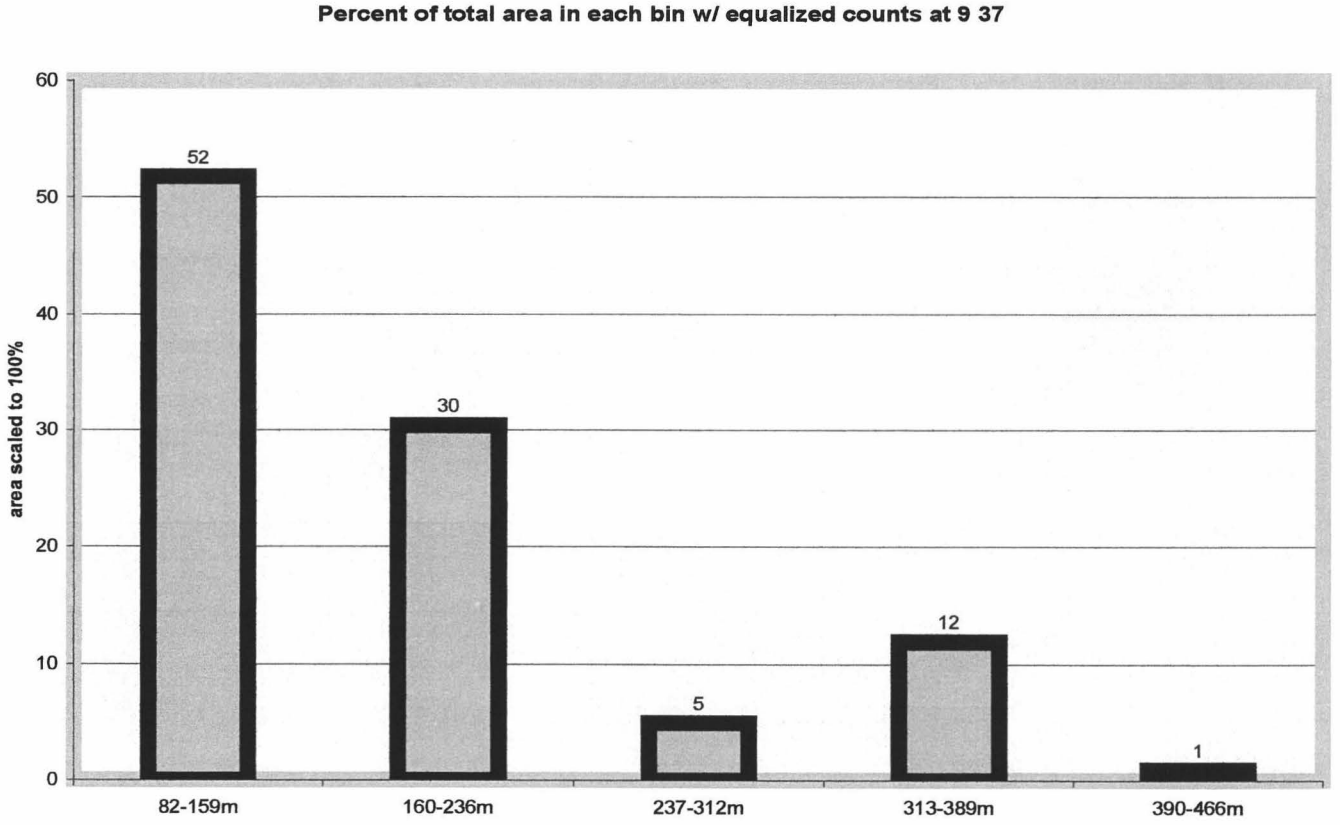
Percent of total area in each bin w/ equalized counts at 9 37
area scaled to 100%
60
50
40
30
20
10
0
52
30
5
12
1
82-159m
160-236m
237-312m
313-389m
390-466m

Figure 14

REFERENCES

Appelgate, B., Embley, R.W., 1991. Submarine tumuli and inflated tube-fed lava flows on Axial Volcano, Juan de Fuca Ridge. Bull. Volcanol., 54, 447-458.

Ballard, R.D., Holcomb, R.T., van Andel, T.H., 1979. The Galapagos Rift at 86°W: Sheet Flows, Collapse Pits, and Lava Lakes of the Rift Valley. Jour. Geophys. Res., 84, 5407-5422.

Barone, A. M., Ryan, W. B. F., 1988. Along-Axis Variations Within the Plate Boundary Zone of the Southern Segment of the Endeavour Ridge. Jour. Geophys. Res., 93, 7856-7868.

Carbotte, S. M., Macdonald, K. C., 1994. Comparison of seafloor tectonic fabric at intermediate, fast, and superfast spreading ridges: Influence of spreading rate, plate motions, and ridge segmentation on fault patterns. Jour. Geophys. Res., 99, 13609-13631.

Chadwick, W.W. Jr., Embley, R.W., Scheirer, D.S., Johnson, H.P., 2000. High-resolution bathymetric surveys using scanning sonars: Relationship between hydrothermal vents and geologic structure at recent eruption sites on the Juan de Fuca Ridge. Submitted to Jour. Geophys. Res.

Chadwick, W.W. Jr., Gregg, T.K.P., Embley, R.W., 1999. Submarine lineated sheet flows: a unique lava morphology formed on subsiding lava ponds. Bull. Volcanol., 61, 194-206.

Chadwick, W.W. Jr., Embley, R.W., 1998. Graben formation associated with recent dike intrusions and volcanic eruptions on the mid-ocean ridge. Jour. Geophys. Res., 103, B5, 9807-9825.

Christeson, G. L., Purdy, G. M., Fryer, G. J., 1992. Structure of young upper crust at the East Pacific Rise near 9°30' N. Geophys. Res. Letters 19, No 10, 1045-1048.

Cochran, J. R., Fornari, D. J., Coakley, B. J., Herr, R., Tivey, M. A., 1999. Continuous near-bottom gravity measurements made with a BGM-3 gravimeter in DSV Alvin on the East Pacific Rise crest near 9 degrees 31' N and 9 degrees 50' N. Jour. Geophys. Res., 104, 10841-10861.

Delaney, J. R., Kelley, D. S., Lilley, M. D., Butterfield, P. A., Wilcock, W. S. D., Embley, R. W., Summit, M., 1998. The quantum even of oceanic crustal accretion; impacts of diking at mid-ocean ridges. Science, 281, 222-230.

Fornari, D. J., Haymon, R. M., Perfit, M. R., Gregg, T. K. P., Edwards, M. H., 1998. Axial summit trough of the East Pacific Rise 9 degrees – 10 degrees N;

geological characteristics and evolution of the axial zone on fast spreading mid-ocean ridges. Journal of Geophysical Research, B, Solid Earth and Planets, 103, 9827-9855.

Fornari, D.J., 1986. Submarine lava tubes and channels. Bull. of Volcan., 48, 291-298.

Fornari, D. J., Embley, R. W., 1995. Tectonic and volcanic controls on hydrothermal processes at the mid-ocean ridge; an overview based on near-bottom and submersible studies. Humphris, S. E. (Ed.) Geophysical Monograph, 91, 1-46.

Fornari, D. J., Spencer, W. D., 1998. Woods Hole Oceanic Institution Towed Camera Sled, Technical and Operations Manual. WHOI Technical Report, 10.

Fox, C. G., Dziak, R. P., 1999. Internal deformation of the Gorda Plate observed by hydroacoustic monitoring. Journal of Geophysical Research, 104, 17603-12616.

Gregg, T.K.P., Fink, J.H., 2000a. A laboratory investigation into the effects of slope on lava flow morphology. Jour. Volcan. Geothermal Res. 96, 145-159.

Gregg, K. P., Fornari, D. J., Perfit, M. R., Ridley, W. I., Kurz, M. D., 2000. Using submarine lava pillars to record mid-ocean ridge eruption dynamics. Earth Planet. Sci. Lett., 178, 195-214.

Gregg, T.K.P., Fink, J.H., 1995. Quantification of submarine lava-flow morphology through analog experiments. Geology, 23, 73-76.

Griffiths, R.W., Fink, J.H., 1992. Solidification and Morphology of Submarine Lavas: A Dependence on Extrusion Rate. Jour. Geophys. Res. Lett., 97, 19,729-19,737.

Haymon, R. M., 1996. The response of ridge-crest hydrothermal systems to segmented, episodic magma supply. MacLeod, C. J. (Ed.) Geological Society Special Publications, 118, 157-168.

Haymon, R.M., Fornari, D., Edwards, M., et al., 1993. Volcanic eruption of the mid-ocean ridge along the East Pacific Rise crest at 9°45'-52'N: Direct submersible observations of seafloor phenomena associated with an eruption event in April, 1991, *Earth Planet. Sci. Lett.*, *119*, 85-101.

Haymon, R.M., Fornari, D.J., Edwards, M.H., Carbotte, S., Wright, D., Macdonald, K.C., 1991. Hydrothermal vent distribution along the East Pacific

Rise crest (9°09'-54'N) and its relationship to magmatic and tectonic processes on fast-spreading mid-ocean ridges. Earth Planet. Sci. Lett., 104, 513-534.

Hon, K., Kauahikaua, J., Denlinger, R., MacKay, K., 1994. Emplacement and inflation of pahoehoe sheet flows: Observations and measurements of active lava flows on Kilauea Volcano, Hawaii. Geo. Soc. of Am. Bull., 106, 351-370.

Humphris, S. E., (Ed.) Seafloor hydrothermal systems; physical, chemical, biological, and geological interactions. Geophysical Monograph, 91, 466.

Kleinrock, M. C., Humphris, S. E., 1996. Structural asymmetry of the TAG rift valley; evidence from a near-bottom survey for episodic spreading. Geophysical Research Letters, 23, 3439-3442.

Klitgord, K. M., Mammerickx, J., 1982. Northern East Pacific Rise; magnetic anomaly and bathymetric framework. Journal of Geophysical Research, 87, 6725-6750.

Klingelhofer, F., Hort, M., Kumpel, H.-J., Schmincke, H.-U., 1999. Constraints on the formation of submarine lava flows from numerical model calculations. Jour. Volcan. Geothermal Res., 92, 215-229.

Kurras, G.J., Fornari, D.J., Edwards, M.H., Perfit, M.R., Smith, M.C., 2000. Volcanic Morphology of the East Pacific Rise Crest 9°49'-52': Implications for volcanic emplacement processes at fast-spreading mid-ocean ridges. Mar. Geophys. Res., 21, 23-41.

Lonsdale, P., 1977. Abyssal pahoehoe with lava coils at the Galapagos Rift. Geology, 5, 147-152.

Macdonald, K. C., Fox, P. J., Miller, S., Carbotte, S., Edwards, M. H., Eisen, M., Fornari, D. J., Perram, L., Pockalny, R., Scheirer, D., Tighe, S., Weiland, C., Wilson, D., 1992. The East Pacific Rise and its flanks 8-18 degrees N; history of segmentation, propagation and spreading direction based on SeaMARC II and Sea Beam studies. Marine Geophysical Res., 14, 299-344.

Moore, J.G., Phillips, R.L., Grigg, R.W., Peterson, D.W., Swanson, D.A., 1973. Flow of Lava into the Sea, 1969-1971, Kilauea Volcano, Hawaii. Geo. Soc. of Am. Bull., 84, 537-546.

Morrissey, M., Zimanowski, B., Wohletz, K., and Buettner, R., 2000. Phreatomagmatic fragmentation. *in* Encyclopedia of Volcanoes, Sigurdsson, H. (ed.) Academic Press, San Diego, CA., pp. 431-445.

Rowland, S. K., Walker, G. P. L., 1990. Pahoehoe and aa in Hawaii: volumetric flow rate controls the lava structure. Bull. Volcanol., 52, 615-628.

Rubin, K. H., 1994. First estimates of elemental fluxes to sea water due to direct evaporation from erupting magmas using (super 210) Po- (super 210) Pb radioactive disequilibrium in recently-erupted 9.5 degrees N EPR lavas. Eos, Transactions, AGU, 75, 618.

Scheirer, D. S., Forsyth, D. W., Conder, J. A., Eberle, M. A., Hung, S. H., 2000. Anomalous seafloor spreading of the Southeast Indian Ridge near the Amsterdam-St. Paul Plateau. Jour. Geophys. Res., 105, 8243-8262.

Schouten, H., Tivey, M. A., Fornari, D. J., Cochran, J. R., 1999. Central anomaly magnetization high: constraints on the volcanic construction and architecture of seismic layer 2A at a fast-spreading mid-ocean ridge, the EPR at 9°30'-50' N. Earth Planet. Sci. Lett., 169, 37-50.

Shah, A., Cormier, M. H., Ryan, W. B., Jin, W., Bradley, A., Yoerger, D., 1999. High resolution 3-D map of the earth's magnetic field at the EPR reveals shallow dike outcrops and large-scale void space in extrusive layers (abstract). Eos Trans., AGU 80 (1999), 1074.

Sharapov, V.N., Pavlov, A.L., Akimtsev, V.A., and Zhmodik, A.S., 2001. Physicochemical conditions of mineral deposition from magmatic gases in basalts of the mid-ocean ridges. Geology of Ore Deposits (translated from Geologiya Rudnykh Mestorozhdenii), v 43, no. 1, 76-87.

Smith, M. C., Perfit, M. R., Fornari, D. J., Ridley, W. I., Edwards, M. H., Kurras, G., Von Damm, K. L., 2000. Magmatic processes and segmentation at a fast spreading mid-ocean ridge: detailed geochemistry and mapping of the East Pacific Rise crest at 9°37' N – a small overlapping spreading center. Submitted to G^3, Dec. 2000.

Sohn, R. A., Hildebrand, J. A., Webb, S. C., 1999. A microearthquake survey of the high-temperature vent fields on the volcanically active East Pacific Rise. Journal of Geophysical Research, 104, 25367-25377.

Stewart, W. K., Chu, D., Malik, S., Lerner, S., Singh, H., 1994. Quantitative seafloor characterization suing a bathymetric sidescan sonar. Jour. Ocean. Eng., 19, 599-610.

Toomey, D.R., Purdy, G.M., Solomon, S.C., Wilcock, W.S.D., 1990. The three-dimensional seismic velocity structure of the East Pacific Rise near latitude 9°30'N. Nature, 347, 639-645.

Tribble, G.W., 1991. Underwater observations of active lava flows from Kilauea volcano, Hawaii. Geology, 19, 633-636.

Vera, E.E., Diebold, J.B., 1994. Seismic imaging of oceanic layer 2A between 9°30'N and 10°N on the East Pacific Rise from two-ship wide-aperature profiles. Jour. Geophys. Res., 99-B2, 3031-3041.

Von Damm , K. L., 2000. Chemistry of hydrothermal vent fluids from 9°-10° N, East Pacific Rise: "Time zero," the immediate post-eruptive period. Jour. Geophys. Res., 105, 11203-11222.

Wadge, G., 1981. The variation of magma discharge during basaltic eruptions. Jour. Volcan. Geothermal Res., 11, 139-168.

Walker, G.P.L., 1971. Compound and Simple Lava Flows and Flood Basalts. Bull. Volcanol., 35, 579-590.

Whitcomb, L. L., Yoerger, D. R., Singh, H, 1999. Advances in doppler-based navigation of underwater robotic vehicles. In Proceedings of the IEEE International Conference on Robotics and Automation, 1, 399-406.

White, S. M., Macdonald, K. C., Haymon, R. M., 2000. Basaltic lava domes, lava lakes, and volcanic segmentation on the southern East Pacific Rise. Jour. Geophys. Res., 105, 23519-23536.

Wohletz, K.H., 1983. Mechanisms of hydrovolcanic pyroclast formation: Grain size, scanning electron microscopy and experimental results. J. Volcanol. Geotherm. Res., 17, 31-63.

Wolfe, E.W., Neal, C.A., Banks, N.G., Dugan, T.J., 1988. Geologic observations and chronology of eruptive events. In Wolfe, E.W., ed., The Puu Oo eruption of Kilauea volcano, Hawaii: Episodes 1 through 20, January 3, 1983, through June 8, 1984. U.S. Geological Survey Professional Paper 1463, 251.

Wright, D.J., Haymon, R.M., Macdonald, K.C., 1995. Breaking new ground: Estimates of crack depth along the axial zone of the East Pacific Rise (9°12'-54'N). Earth Planet. Sci. Lett., 134, 441-457.

Yoerger, D. R., Cochran, J. R., Fornari, D. J., Herr, R., McGee, T., Schouten, H., Tivey, M. A., 2000. Near-bottom, underway gravity survey of the small overlapping spreading center at 9°37' N on the East Pacific Rise crest (abstract). Eos Trans., AGU 81, 1077.